Carbon 248 (2026) 121162

Contents lists available at ScienceDirect

Carbon

journal homepage: www.elsevier.com/locate/carbon

Competing conduction mechanisms in high performance carbon nanotube fibers

John Bulmer [a,b,*], Chris Kovacs [b], Thomas Bullard [b], Charlie Ebbing [b], Timothy Haugan [b], Ganesh Pokharel [c,d], Stephen D. Wilson [d], Fedor F. Balakirev [e], Oscar A. Valenzuela [e], Michael A. Susner [f], David Turner [f], Pengyu Fu [g], Teresa Kulka [h], Jacek Majewski [h,i], Irina Lebedeva [j,k], Karolina Z. Milowska [j,l], Agnieszka Lekawa-Raus [m], Magdalena Marganska [n,o]

[a] University of Cincinnati, 598 Rhodes Hall, P.O. Box 210072, Cincinnati, OH, USA
[b] Aerospace Systems Directorate, Air Force Research Laboratory, Wright-Patterson Air Force Base, OH, 45433, USA
[c] Perry College of Mathematics, Computing and Sciences, University of West Georgia, Carrollton, GA, 30118, USA
[d] Materials Department, University of California, Santa Barbara, CA, 93106, USA
[e] National High Magnetic Field Laboratory, Los Alamos National Laboratory, Los Alamos, NM, 87545, USA
[f] Materials and Manufacturing Directorate, Air Force Research Laboratory, Wright-Patterson Air Force Base, 2179 12th Street, Ohio, 45433, USA
[g] The Center for High Performance Power Electronics, The Ohio State University, Columbus, OH, 43210, USA
[h] Institute of Theoretical Physics, Faculty of Physics, University of Warsaw, Pasteura 5, PL-02093, Warsaw, Poland
[i] Terahertz Research and Application Center CENTERA2, Center of Advanced Materials and Technologies CEZAMAT, Warsaw University of Technology, Poland
[j] CIC NanoGUNE, Donostia-San Sebastián, 20018, Spain
[k] Simune Atomistics, Donostia-San Sebastián, 20018, Spain
[l] Ikerbasque, Basque Foundation for Science, Bilbao, 48013, Spain
[m] Centre for Advanced Materials and Technologies (CEZAMAT), Warsaw University of Technology, Warsaw, Poland
[n] Institute of Theoretical Physics, Wrocław Tech, Wybrzeże Wyspiańskiego 27, 50-370, Wrocław, Poland
[o] Institute for Theoretical Physics, University of Regensburg, 93040, Regensburg, Germany

ARTICLE INFO

Keywords:
Carbon nanotube
Bundles
Junctions
Electrical conductivity
Magneto-resistance
Heterogeneous transport

ABSTRACT

The performance of carbon nanotube (CNT) cables, a contender for copper-wire replacement, is tied to its metallic and semi-conducting-like conductivity responses with temperature; the origin of the semi-conducting-like response however is an underappreciated incongruity in literature. With controlled aspect-ratio and doping-degree, over 61 unique cryogenic experiments including anisotropy and Hall measurements, CNT cable performance is explored at extreme temperatures (65 mK) and magnetic-fields (60 T). A semi-conducting-like conductivity response with temperature becomes temperature-independent approaching absolute-zero, uniquely demonstrating for the first time the necessity of heterogeneous fluctuation induced tunneling; complete de-doping leads to localized hopping, contrasting graphite's pure metallic-like response. High-field magneto-resistance (including novel +22 % longitudinal magneto-resistance near room-temperature) is analyzed with hopping and classical two-band models, both yielding a similar parameter useful for conductor development. Varying field-orientation angle uncovers significant two- and four-fold symmetries that are shown to be from Aharonov-Bohm-like corrections to the curvature-induced bandgap, a first for macroscale CNT fibers. Tight-binding calculations using Green's Function formalism model the largest, coherent transport to-date in commensurate CNT bundles in magnetic-field, revealing non-uniform transmission across bundle cross-sections with doping restoring uniformity; independent of doping, transport in bundle-junction-bundle systems are predominantly from CNTs adjacent to the other bundle—demonstrating that smaller bundles are more efficient for electronic transport. The final impact is predicting the ultimate conductivity of heterogeneous CNT cables using temperature and field-dependent transport, surpassing conductivity of traditional metals.

* Corresponding author. University of Cincinnati, 598 Rhodes Hall, P.O. Box 210072, Cincinnati, OH, USA
E-mail address: bulmerjn@ucmail.uc.edu (J. Bulmer).

https://doi.org/10.1016/j.carbon.2025.121162
Received 31 October 2025; Received in revised form 28 November 2025; Accepted 14 December 2025
Available online 17 December 2025

1. Introduction

The performance of carbon nanotube (CNT) conductors is steadily improving and now approaches [1–10] copper's specific conductivity and conventional carbon-fiber's tensile-strength [11–13], with continued development expected with greater aspect-ratio [14–16] and incorporating dopants with large-scale order [17]. Older, more fragile, carbon-based conductors however, such as graphitic-intercalation-compounds (GICs) [18], have higher conductivities (50 % greater than copper in absolute terms [19,20]) and, along with its highly-ordered graphite host, have a completely metallic-like resistance R temperature T response ($dR/dT > 0$) down to liquid-helium temperatures [18]. Despite individual metallic CNTs [21] and some CNT bundles [22] also having this full metallic-like $dR/dT > 0$, it is established [15,23–27] that CNT materials with aligned microstructure typically have both a semi-conducting-like response ($dR/dT < 0$) at colder temperatures and a metallic-like response at higher temperatures ($dR/dT > 0$), forming a u-shaped R vs T plot. Moderately ordered graphite [18,28,29] and conductive-polymers [23,30,31] also have this u-shaped response, where the semi-conducting component is from extrinsic factors (junctions, voids and misalignment); when minimized, higher room-temperature conductivity is achieved [23,31]. When finally a conductive-polymer was fabricated with full $dR/dT > 0$, its conductivity was regarded as a pinnacle limit [32,33]. Despite 25 years of CNT-conductor development, a CNT-conductor with a full $dR/dT > 0$ is not yet realized.

The semi-conducting-like $dR/dT < 0$ contribution in CNT-conductors is an underappreciated controversy in literature, where studies pick from either homogeneous transport (variable-range-hopping, insulator-to metal-transition, or weak-localization) or heterogeneous transport (fluctuation-induced-tunneling combined with metallic conduction) without possibly full consideration of other mechanisms. Homogeneous transport, prevalently applied to disordered materials, assumes disordered uniformity with one governing characteristic length. With variable-range-hopping (VRH) for example, widely applied for lower conductivity CNT materials, charge carriers are localized over the characteristic length a and tunnel to distant sites with matching energies (opposed to nearest neighbors with phonon exchange) resulting in exponentially diverging R as $T \to 0$ according to [34–39].

$$R[T] = R_c \, exp\left[\left(\frac{T_M}{T}\right)^{\frac{1}{D+1}}\right] \quad (1)$$

where R_C is a fitting prefactor, D is the dimensionality, and T_M is the Mott temperature (Fig. 1a). T_M is the maximum temperature where VRH applies with $T_M = C/(k_b N(\varepsilon_F) a^D)$ and $C = 18.2$ for $D = 3$ [40,41], $C = 13.8$ for $D = 2$ [42], k_b is Boltzmann's constant, and $N(\varepsilon_F)$ is the density of states at the Fermi level. Above T_M, the semi-conducting-like component becomes Arrhenius thermal-activation. As material order improves (say, by increasing chemical doping [25] or CNT metallicity [43]), $a \to \infty$ and the material undergoes an insulator to metal transition. Now, the homogeneous transport is weak-localization (WL) where the phase-coherence length (L_{Phase}) becomes the limiting characteristic length. Here, electron backscatter from crystal defects adds coherently over L_{Phase} and leads to a small resistance increase (<1 % for 8 nm thin

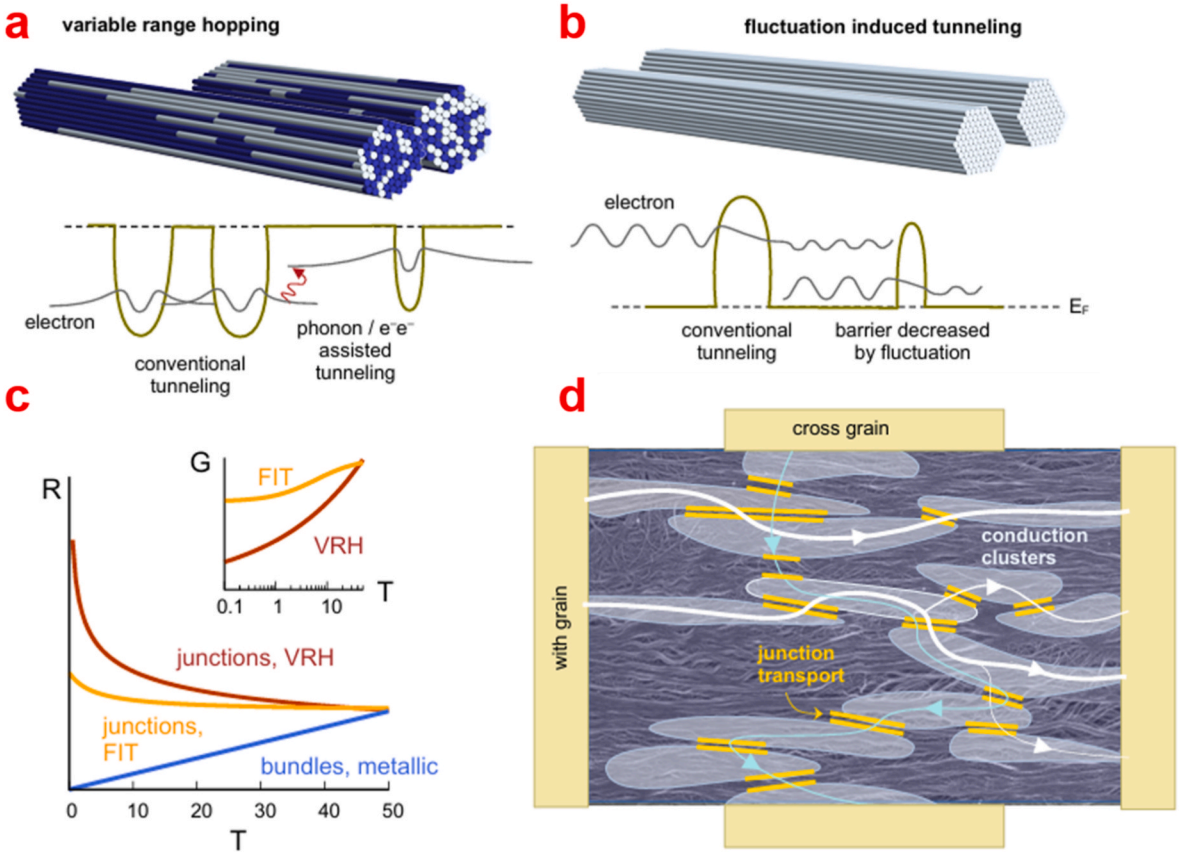

Fig. 1. Proposed heterogeneous CNT network. a, de-doped bundles of mixed semi-conducting (dead-weight, dark blue) and metallic CNTs (light blue); junctions are modeled as variable-range-hopping (VRH) where localized charge carriers tunnel to distant locations with matching energy. b, With as-is (doped), all CNTs participate and junctions are modeled with fluctuation-induced-tunneling (FIT), where long delocalized conduction paths are separated by small insulating gaps. Thermal fluctuations enhance transmission, but are not necessary. c, cartoon of the models' temperature-dependent resistances, with inset showing conductivity. d, SEM photograph of CNT ribbon superimposed by a sketch of metallic conduction paths (with and against microstructure-alignment) with interrupting yellow semi-conducting junctions. (For interpretation of the references to color in this figure legend, the reader is referred to the Web version of this article.)

Cu films at 4 K [44], <3 % for pre-graphitic carbon-fibers at 4 K [45]). Temperature impedes the phase-coherence leading to a gradual $dR/dT < 0$. Weak-localization originally explained the anomalous resistance correction and -MR in metal thin-films [44,46], and later carbon-fiber [45,47], graphitic-intercalation-compounds [48], and CNTs [25,27,43,49–55].

Other CNT studies, somewhat separately, use heterogeneous transport models, comprised of independent mechanisms that combine in some way, for more complex R/T responses. Substantiated by thermopower measurements [56], the R/T u-shape is extrinsically-tunable based on heterogeneous composition, opposed to an intrinsically-fixed material property. The room-temperature resistance of transparent, unaligned CNT films, for example, was estimated by series addition of CNT resistance with CNT junction resistance [57–61]. Temperature-dependent resistance was modeled for unaligned armchair CNT films [62] by a phonon-assisted tunneling term added in series with a hopping term. Fluctuation induced tunneling (FIT) [63] is another empirical-based heterogeneous transport mechanism typically used for u-shape R/T responses where small insulating junctions separate long conductive structures (Fig. 1b). If junction capacitance is sufficiently small, relative to the long conductive structure capacitance, thermal noise voltage fluctuations become sufficient to modify the tunneling potential. This results in the temperature-dependent resistance [23,63]:

$$R(T) = R_c \, exp\left[\frac{T_1}{T + T_2}\right] + R_{metallic}[T] \quad (2)$$

with fitting constant R_c, k_bT_1 the approximate energy barrier of the junction, T_2 is the temperature above which thermal noise becomes important, and $R_{metallic}[T]$ is the system-specific long conductive structure resistance. Note that FIT represents junctions between CNT structures and has the simplest mathematical form to generate constant resistance when $T << T_2$ (signaling temperature-independent tunneling), while generating Arrhenius-style thermal-activation when $T >> T_2$. Equation (2) has been applied to conductive-polymers [64], CNT-conductors [24,27,37,55,65], and individualized metal-nanowires (where controlled metal-nanowires form a single junction for FIT model validation [66,67]). Magnetic-field dependence is not yet established [37] and, anecdotally, FIT is not widely utilized outside of the polymer community. A sketch of $R(T)$ for the metallic (bundle transport) and junction (VRH and FIT for de-doped and as-is CNTs, respectively) is shown in Fig. 1c, with an inset showing the junctions' conductance $G(T)$. A schematic illustration of the CNT fiber with the conducting regions separated by junctions is shown in Fig. 1d. Considering more extreme conditions (to include ultracold temperatures, high magnetic field, and completely de-doped CNTs) could enable more decisive selection of transport mechanisms that is largely split in literature (as discussed above) and identify bottlenecks for continued improvement in CNT-conductors.

In this work, we systematically vary aspect-ratio and doping-degree in the latest CNT-conductors (solution-spun fiber and ribbon, over 61 distinct cryogenic measurements) and uniquely explore the most extreme temperatures (<65 mK) and magnetic-fields (60 T, multiple orientations) that have ever been attempted in this CNT-conductor class. Experiments are compared with coherent tight-binding transport simulations for an individual CNT rotating in magnetic-field, as well as the largest-ever simulations of coherent transport in spatially-extensive CNT bundles. We systematically compared empirical homogeneous and heterogeneous transport models, contrasting most literature that generally selects some transport models without full consideration of others (broadly speaking, there is an underappreciated rivalry between VRH/WL vs. FIT as discussed above). This work is noteworthy because, for the first time: 1) Correlations between CNT-conductor performance, structure, and temperature-response are now thoroughly established; underscoring that understanding and control of transport mechanisms is possible and desirable. 2) While conceptually proposed long ago, heterogeneous transport (in particular, FIT) is experimentally demonstrated as an unavoidable necessity as the dominant contribution to CNT-conductor resistance, with heterogeneous resistance terms adding in series; this opens a method to determine the ultimate CNT-conductor conductivity. 3) We discover high-field (60 T) positive quadratic magneto-resistance without saturation; likely classical in nature, this is relevant as more traditional Hall measurements struggle with heterogeneous materials. 4) Rotating the CNT-conductor in magnetic field reveals novel two- and four-fold symmetries in the magneto-resistance oscillation, convincingly attributed to quantum Aharonov–Bohm (AB) corrections never before applied to bulk CNT materials. 5) First-ever simulations on large bundles show complex cross-sectional transmission distributions, while doping makes transmission uniform independent of CNT electronic species. For a bundle-junction-bundle series, independent of the doping level, only adjacent CNTs in the other bundle participate in the transport. Importantly, this demonstrates how smaller diameter bundles are more efficient within a CNT conductor. A well-narrated database [68] exhaustively provides the complete cryogenic and room-temperature property data, as well as model-fitting, correlation tables, and literature-based compendium of MR mechanisms.

2. Methods

Database. All data is organized and provided in this database [68]. Also included are material property correlation tables (p-values <0.05 were statistically significant) and a compilation of the transport models fits. Linear regression and non-linear curve fitting was accomplished in OriginPro where error was propagated to calculate a reduced X^2 for model comparison.

Materials. Provided from Dexmat, aligned CNT ribbons and fibers were made from the established [1,14] method of wet-spinning solutions of chlorosulfuric acid (CSA) and CNTs through a spinneret into a coagulant, such as acetone or water. The CNTs were few-walled and of high graphitic quality; this was verified by Raman spectroscopy showing radial breathing modes (RBMs) and a high G:D ratio (supplemental-Fig. 1.2-1). After the 1000 °C H_2 bakeout, Raman spectra became sharper and there was no degradation of the G:D ratio. Scanning electron microscopy shows the degree of microstructure-alignment (supplemental-Fig. 1.1-1). Thermogravimetric analysis (TGA) showed residual iron content <0.6 % and X-ray fluorescence showed surface iron contamination was <0.1 % (Supplemental-Fig. 1.3-1–2). CNT ribbons and fibers were composed of CNTs with company-controlled molecular aspect-ratios, to include 5600, 4800, 3100, and 1200. These aspect-ratios were verified by dissolving the CNTs back into CSA solution and conducting extensional rheometry [69].

Physical Property Measurement System. CNT-conductors were measured in a Quantum Design Physical Property Measurement System (PPMS) using a standard four-wire resistance technique with probe-wires mounted with silver paint (ribbons were typically 1 cm long, 1–2 mm wide, 4–5 mm between inner leads). Sample resistances ranged from 0.02 to 0.16 Ω (as-is ribbons), 0.1–2 Ω (de-doped ribbons), 0.5–37 Ω (CNT fibers, as-is and de-doped) with temperatures ranging from 1.9 to 373 K. Different probe-currents were used for a sample run (20 μA, 100 μA and 1000 μA) where trace overlap indicated sample heating was not an issue; the DC current switched directions to remove thermoelectric effects. When used, the DC magnetic-field (9 T max) was applied normal to the surface of the CNT sample and consequentially perpendicular to both the probe-current and CNT microstructure-alignment. In some circumstances a specialized probe holder was used to continuously rotate the CNT sample in the static magnetic-field. 0° indicates that the magnetic-field is perpendicular to the sample surface, 90° indicates the magnetic-field is parallel to the sample surface. The sample first rotated without any magnetic-field to generate a base line (supplemental-Fig. 4.3-10). For resistance measurement for temperatures between 0.05 and 3.8 K, select CNT ribbons were measured using a separate Quantum Design Dynacool PPMS equipped with a dilution refrigerator (DR) insert

and Electrical Transport Option (ETO) module. An in-situ cryo-clean was made for optimal performance of the DR, especially to stabilize the temperature at ultra-low temperatures. Probe-currents ranged from 10 to 50 mA without signs of heating. Temperature ramp rate was 0.025 K/min to ensure sample thermo-equilibrium. Both 0 T and 14 T were applied with magnetic-field normal to the CNT ribbon surface.

High-Pulsed Field. Four-wire probe magneto-resistance measurements up to 60 T (≈9 ms rise, 30 ms fall) were accomplished with a pulse magnet at the National High Magnetic Field Laboratory (NHMFL), Los Alamos National Laboratory (LANL). Two samples of each CNT ribbon category were measured simultaneously for redundancy. Samples were hooked up to fine magnet wires with silver paint, with care taken to minimize wire loops and anchor wires to the supporting structure with GE varnish, to minimize vibration. Probe-current was always in the direction of microstructure-alignment and the magnetic-field was typically perpendicular to the sample surface (transverse MR) and one sample run had magnetic-field parallel to the probe-current and microstructure-alignment (longitudinal MR). The magnetic-field was measured by a calibrated B-dot probe inductor, which was also used to precisely align the sample in the magnet's center when installing the sample. Supplemental-Fig. 3.1-1 shows the measurement circuit. An AC signal with frequency above the magnet noise (typically either 32 kHz or 175 kHz) drove current through the sample, with sample voltage sent through a Stanford Instruments SR560 Preamp (typically 1000x amplification, 10–300 kHz bandpass), before digitization recording (3.2 MS/s). A 10.2 Ω was put in series with the sample to probe the sample current, where its voltage drop was measured in a similar way. A post-process lock-in amplifier technique isolated the sample resistance from electromagnetic noise. A magnetic pulse measurement was accomplished for multiple temperature setpoints from 1.45 to 270 K. For the de-doped CNT ribbons, before measurement, a bake-out for ≈100 °C, 1 h under vacuum was also accomplished within their measurement housing.

Model of orbital response in magnetic-field. The construction of the appropriate effective Hamiltonian, describing the physics of the bands close to the charge-neutrality point, is discussed in the Supplemental-section 5.1. Its main parameters are the initial small bandgap (2.2 meV) and the magnitude of the orbital magnetic moment (0.323 meV/T); they were estimated from the fact that at high temperature the strongest -MR in de-doped fibers occurs at $H_{||,0} \approx 3.4$ T (Fig. 4a and b) and from the value of $d \approx 1.5$ nm measured in Raman spectroscopy. The reason why we used high temperature data for parameter extraction is that the experimental situation may be complicated by an additional contribution to MR from weak-localization; but between 30 K and 60 K the strongest -MR remains at 45°, so the weak-localization is likely already suppressed. The conduction through an individual nanotube, needed to assess the magneto-resistance, has been calculated using the Landauer-Büttiker approach with the energy spectrum given by the effective model.

Tight-binding bundle modelling. The spin-unpolarised tight-binding calculations of SWCNT bundles and bundle junctions were carried out using the sisl Python library [70] and TBtrans [71]. Together, these codes enable the construction of tight-binding Hamiltonians and the use of Peierls substitution to account for the orbital effects of strong magnetic fields, while TBtrans employs the non-equilibrium Green's function (NEGF) formalism for transport calculations. In our work we employed a locally modified version of TBtrans, based on version 5.2.0-alpha of SIESTA code [71], to enable full Peierls substitution in both the Hamiltonian and overlap matrices (H and S) of the device and electrodes. This modification is essential for reproducing all results presented here. The complete implementation details are provided in Supplemental Section 5.2.

3. Results

We obtained ribbons and fiber composed of high-quality few-wall CNTs with aligned microstructures from Dexmat using the established acid-solution spinning-process [1,14] with different molecular aspect-ratios (AR: 1200, 3100, 4800, and 5600). These CNT materials are p-doped from their acid-based production process (labeled "as-is"), which we can remove with a 1000 °C 1-h bakeout in flowing H_2. Afterwards laboratory air and moisture re-exposure lightly p-dopes the de-doped CNT-conductor [72,73], so we also implemented a 100 °C vacuum bake-out within every electrical characterization apparatus to remove the physisorbed species [43,74] (Labeled "de-doped", further details in supplemental-section 1.0). Four-wire resistance, either with or perpendicular to the microstructure-alignment, was measured in Quantum Design Physical Properties Measurement System (PPMS) from room-temperature down to 1.9 K, with magnetic-field up to 9 T and the ability to change sample orientation in field. In two cases, a different PPMS system enabled measurement down to <65 mK and fields up to 14 T. Resistance was converted to a specific-conductivity for easier comparisons across samples, which is a more useful metric than standard conductivity because a cross-sectional area, which is variable in porous materials, is not required for calculation [15].

Temperature-dependent conductivity. Compiling all 28 zero-field cryogenic resistance measurements, Fig. 2a plots the room-temperature specific-conductivity σ across all samples (ribbon, fibers, as-is, and de-doped) against their cryogenic-resistance-ratio (resistance at 300 K divided by resistance at 10 K). Specific-conductivity values measured either in parallel or perpendicular microstructure-alignment have the same linear relationship, although parallel is on average 20x higher (Supplemental-Fig. 2.2-4). A CNT meta-analysis also demonstrated similar correlation across many studies [15]. These correlations demonstrate that understanding and controlling the metallic-like and semi-conducting-like temperature responses leads to improved performance. Fig. 2b plots aspect-ratio versus cryogenic-resistance-ratio, showing positive correlation for as-is (r>90 %). These aspect-ratios correspond to CNT lengths 1.8, 4.65, 6.75, and 8.4 μm (assuming a 1.5 nm diameter CNT), which is greater than the characteristic lengths in homogeneous transport models: an individual CNT's phonon-limited mean-free-path (1 μm at room-temperature [75]); phase-coherence-length (10–40 nm from 100 to 2 K[76]) in weak-localization; localization lengths (<6 nm [41,76]) in VRH. This supports the thesis that the cryogenic-resistance-ratio is dictated by a heterogeneous network of CNT structures and junctions, opposed to homogeneous transport mechanisms. De-doping categorically decreases the cryogenic-resistance-ratio (on average, by a factor of 3, Fig. 2b and Supplemental-Fig. 2.2-3), while any upward trends with aspect-ratio are no longer statistically significant. This correlation loss indicates a different transport regime primarily controlled just by junctions.

Fig. 2c shows specific examples of specific-conductivity (parallel microstructure-alignment) versus temperature with aspect-ratio and doping-status indicated, all showing the upside-down "u" profile familiar from literature [15,23–27]. The as-is has a pronounced metallic-like component ($d\sigma/dT < 0$) compared to its semi-conducting-like component ($d\sigma/dT > 0$), where the semi-conducting component notably levels-off to a constant value approaching absolute-zero. This conclusive level-off, shown for the first time for these high-performance CNT-conductors at particularly low temperatures (<65 mK), validates their fundamentally metallic nature. Transverse DC magnetic-field (H, depicted up to 14 T with different colors) shows a small positive conductivity contribution. The semi-conducting component under field still remains, however, implying an origin not from weak-localization (which is suppressed by field).

The dependence on aspect-ratio, with CNT length far greater than typical homogeneous characteristic lengths, implies heterogeneous transport with independent terms for CNT structures and their junctions; further, the upside-down u-shape with one maximum implies a total resistance that is the series sum of one metallic-like resistance term and one semi-conducting-like resistance term. The heterogeneous transport

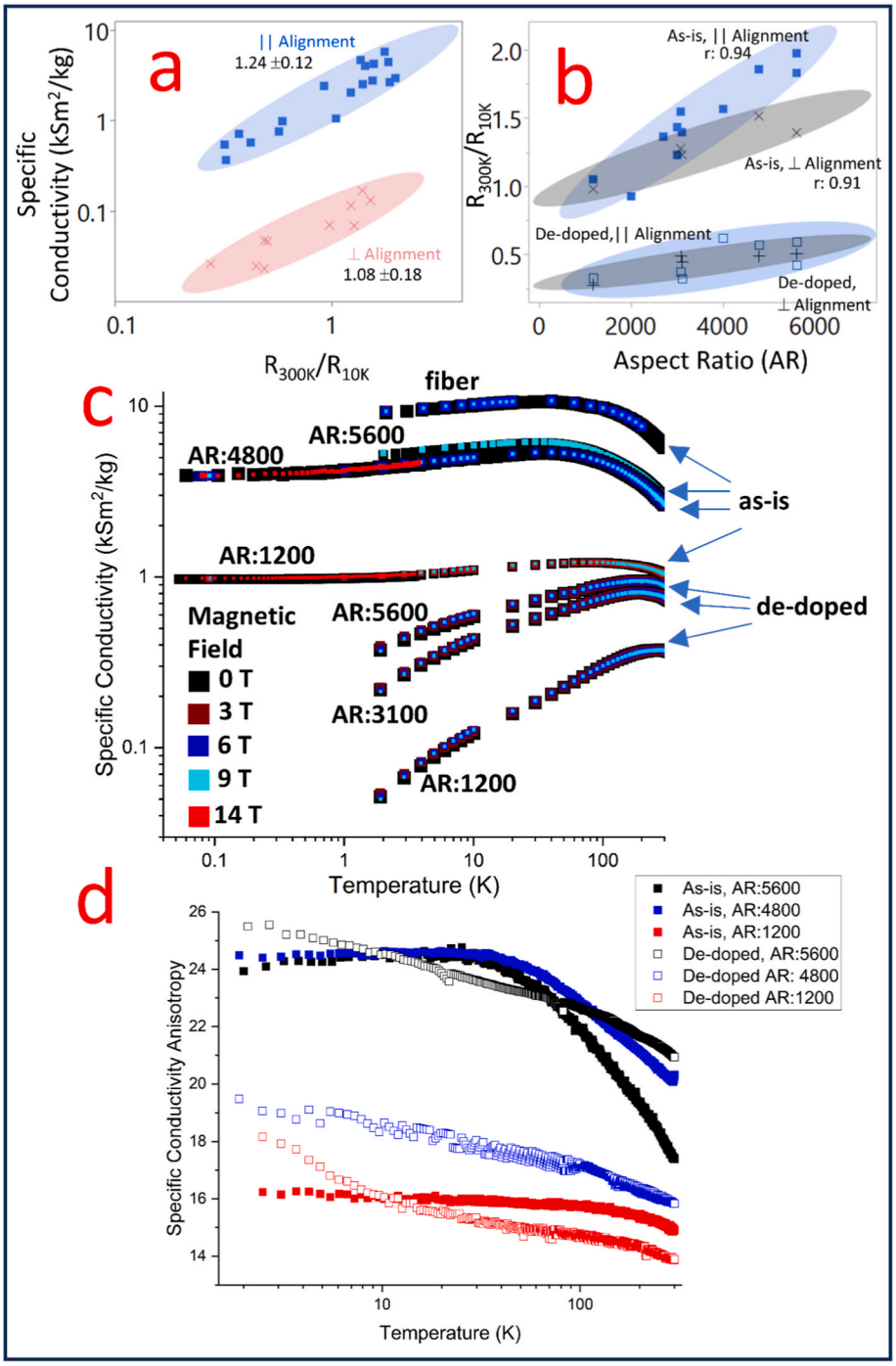

Fig. 2. Conductivity temperature dependence. a, zero-field room-temperature specific-conductivity versus cryogenic-resistance-ratio (R at 300 K/R at 10 K) across all materials, with partitioning according to microstructure-alignment, with power-law exponent. b, cryogenic-resistance-ratio versus aspect-ratio (AR) partitioned by doping-status and microstructure-alignment, with correlation indicated for as-is. c, Specific examples of parallel-alignment specific-conductivity vs temperature for various AR and doping-status. Colors represent the transverse magnetic-field H. d, temperature-dependence of the specific-conductivity anisotropy. (For interpretation of the references to color in this figure legend, the reader is referred to the Web version of this article.)

model FIT (equation (2)) is consistent with the conductivity level-off approaching absolute-zero. The best FIT fits were with adding a metallic power-law resistivity term ($R_{metallic}[T] \propto T^x$ with exponent x between 1.4 and 2.5), opposed to a more standard linear or quasi-1D metallic term [77]. Correlations with the heterogeneous fits are shown in Supplemental-section 2.3.

De-doped CNT-conductors are less conductive (on average, 6x lower, Supplemental-Fig. 2.2-2) and have a greater semi-conducting component that, rather than level-off, rapidly approaches zero conductivity approaching absolute-zero. Reduced-activation-energy analysis and fitting to specific VRH models (Supplemental section 2.1) indicates the insulator side of the metal/insulator transition with typically 3D VRH. If the de-doped sample was not vacuum-baked within the measurement apparatus, it would be on the metal/insulator transition (indicated by power-law dependence between conductivity and temperature approaching absolute-zero), rather than hopping conduction [25]. This is similar to earlier reports on de-doped CNT fibers [25] and contrasts the fully metallic temperature response of high-quality graphite

[78–80]. Note that the de-doping post-process does not negatively impact the CNT structure itself (Supplemental-section 1.0). Despite VRH at colder temperatures, above ≈200 K a small metallic-like component appears ($d\sigma/dT < 0$). Similar to as-is, the u-shaped mixed metallic/semi-conducting components indicate a heterogeneous mixture of junctions and CNT structures, which is expected considering the CNT lengths and typical VRH localization lengths (4.6–9 nm [34,36,39,41]). Dissimilar to as-is, we saw that the cryogenic-resistance-ratio was not significantly correlated to aspect-ratio and this indicates a difference in junction mechanisms. As suggested in Ref. [43], the completely de-doped semi-conducting CNTs are essentially always insulating (for $d = 1.5$ nm, semi-conducting bandgap ≈233 meV, corresponding to a thermal-activation of 2700 K); therefore, the de-doped metallic CNTs are always responsible for electrical conductivity over the temperature range of interest (65 mK–300 K) and the network is now more sparse and percolative relative to the as-is/highly-doped case where all CNTs can contribute.

Fig. 2d shows the specific-conductivity anisotropy versus temperature for CNT ribbons, defined as the ratio of specific conductivity with the current flowing with-grain to that with the current flowing across-grain. With decreasing temperature for as-is, the specific-conductivity anisotropy first increases and then becomes constant below ≈100 K. This level-off is also reflected in the fitted parameters for FIT, where T_1 and T_2 do not differ significantly between parallel and perpendicular cases (Supplemental-section 2.3). De-doped changed gradually with temperature without this level-off. The change of anisotropy all-together however was never large (from 300 K to 2 K, the change was <33 %). Temperature independence of conductivity anisotropy has been observed before in aligned CNT materials [81]; it was concluded there was no fundamental difference in junction or CNT transport in different directions and that anisotropy manifested by the extrinsic differences in the parallel and perpendicular geometries of the larger percolating network. This contrasts graphite where conductivity anisotropy, in one case, was 12.5 at room-temperature and increased to 54 at cryogenic temperatures [82]; this also contrasts the quasi-1D metal tetrathiofulvalinium tetracyanoquinodimethan (TTF)(TCNQ) going from 500 at room-temperature to 10,000 at cryogenic temperatures [83]. Considering our anisotropy changes little with temperature implies the current distribution through the CNT structure-junction network is also changing little with temperature. In other words, if tributary parallel connections became relevant at higher temperature, less tortuous paths against-the-grain would be taken at higher temperature; then, the anisotropy would be closer to 1 at higher temperature and more extreme at cold temperature. Indeed, this behavior is observed on a small scale, relative to the overall resistance change, and demonstrates the impact of tributary parallel connections is small. This smallness in anisotropy change supports heterogeneous transport models where CNT-conductor resistance is a series sum of CNT structure resistors and junction resistors, without tributary parallel connections (e.g., equation (2)). See supplemental-section 2.2 for additional correlations, reduced-activation-energy-analysis, VRH and FIT fitting.

High-field positive (+) MR. High-field magneto-resistance ($MR(H)$

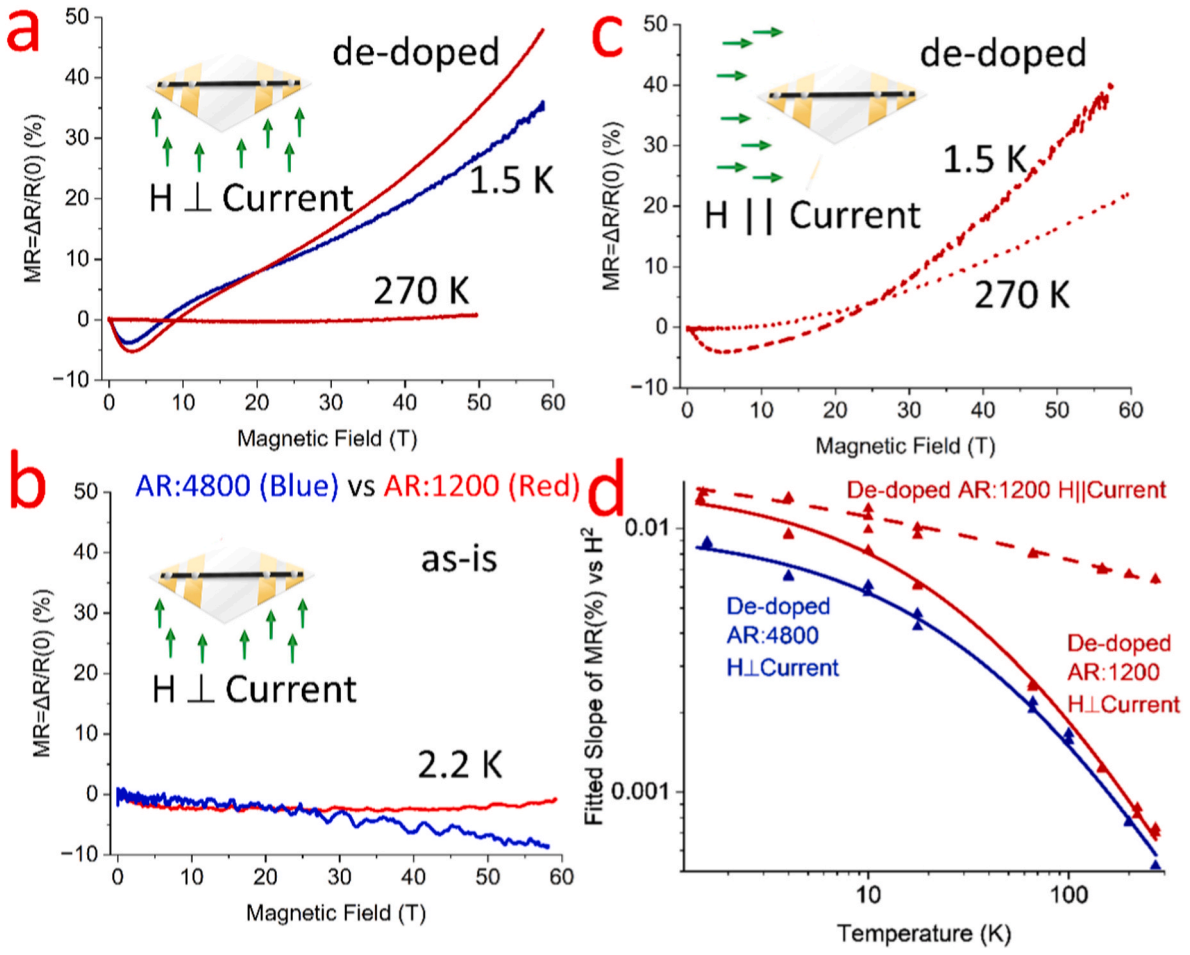

Fig. 3. High-field magneto-resistance (MR(%) = 100 % ($R(H)$-$R(0)$)/$R(0)$) versus magnetic-field H, for select temperatures T for short (AR: 1200, red) and long (AR: 4800, blue) aspect-ratios (AR) and probe-current always || CNT alignment. a, de-doped with $H \perp$ CNTs. b, as-is with $H \perp$ CNTs. c, de-doped now with H || CNTs. d, just for de-doped, plotting the fitted slope of MR vs H^2 coefficient against T, which is useful for VRH and classical two-band analysis. (For interpretation of the references to color in this figure legend, the reader is referred to the Web version of this article.)

= 100 %*(R(H)-R(0))/R(0), sweeping magnetic-field H up to 60 T and measuring four-wire resistance R) was accomplished with a pulse magnet at National High Magnetic Field Laboratory; Fig. 3 shows *MR* versus H for select aspect-ratios (AR) and temperature T. De-doped CNT-conductors under transverse-field (Fig. 3a) have an initially negative (−) MR, followed by + MR to an inflection point at ≈10 T, where + MR continues and is broadly quadratic (MR: 48 % at 1.5 K, 60 T) without saturation. Near room-temperature, the +MR is smaller though still present (MR: 0.8 % at 270 K, 50 T). In contrast, as-is (Fig. 3b) lacks positive quadratic MR. Further, for as-is and de-doped, there is no obvious qualitative difference between the 4800 and 1200 aspect-ratios. These results resemble our previous high-field MR of CNT-conductors from direct spinning, where CNTs are considerably longer [27,84], although are more heterogeneous and porous; this highlights that our MR response applies to varieties of CNT-conductors. Notably, large longitudinal MR (Fig. 3c, H now parallel to current and CNT alignment, MR goes up to 41 % at 1.5 K and 22 % at 270 K) matches or exceeds the transverse MR (H perpendicular to current). While this particular longitudinal sample was de-doped by our standard 1000 °C hydrogen treatment, because of logistical constraints, our 100 °C vacuum bake-out within the magnet did not occur. This means there was some light-doping from atmosphere physisorption and the +MR could be even greater if fully de-doped. Compiling all de-doped results onto one graph, Fig. 3d plots temperature against the fitted straight-line slope of +MR vs H^2. This fitted slope monotonically decreases with temperature where transverse MR subsides faster than longitudinal (unabridged high-field MR, Supplemental-section 3.0).

High-field + MR under VRH. The high-field + MR increases quadratically without saturation and this discourages explanations using anisotropic magneto-resistance (AMR) dealing with magnetic impurities [85–87] or field-induced spin polarization mechanisms [27, 88]. Zeeman splitting becomes relevant when $g u_B H > k_b T$, where $g \approx 2$ is the g-factor, and u_B is the Bohr magneton; increased charge carrier interaction from Zeeman splitting causes + MR for other carbon-based

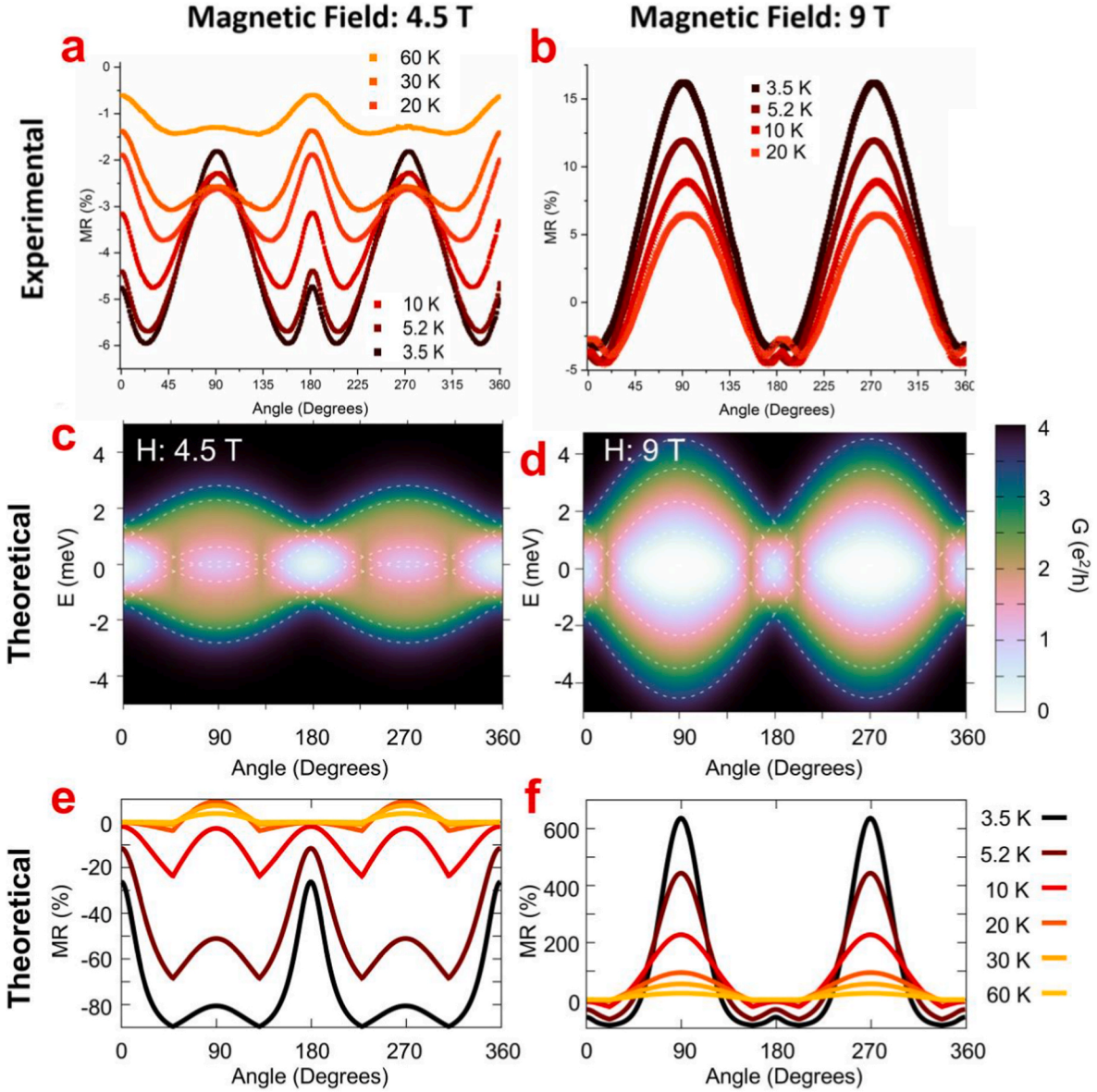

Fig. 4. a, MR modulation of a de-doped CNT fiber as it continuously rotates in steady field $H = 4.5$ T, with probe-current always || CNT microstructure-alignment. 0° represents H⊥CNTs and 90° represents ||. b, the same except at 9 T. c, tight-binding simulation of the AB-modified curvature-induced bandgap versus field-angle, for an individual non-armchair metallic single-wall CNT, with $H = 4.5$ T and $T = 3.5$ K. Color represents transmission in units of quantum conductance ($G = e^2/h$). d, the same except $H = 9$ T. e, Slicing the band-diagram at the Fermi level ($E_f = 0$) allows MR (%) calculation, qualitatively reproducing the experimental results. (For interpretation of the references to color in this figure legend, the reader is referred to the Web version of this article.)

conductors [54,89–91], although is regarded as a liquid-helium phenomena and does not explain the +MR near room-temperature. With transverse MR, for our CNT diameters ($d \approx 1.5$ nm), H is too small for Landau levels where ≈1000 T is required for significant + MR [92–96]. Note that only CNT-conductors with high-field + MR, the de-doped ones, also follow VRH. A well-known [40,97–99] VRH MR mechanism predicts approximately quadratic + MR via H-induced constriction of the localized wavefunction; this leads to reduced hopping and lower conductivity, with a power-law temperature-dependence [40,42]:

$$MR(\%) = 100\% \frac{t\, e^2 a^4}{\hbar^2} \left(\frac{T_M}{T}\right)^s H^2 \tag{3}$$

where a is the charge carrier localization-length, e electron charge, $\hbar$ is reduced Plank's constant, $t = 0.00248$, and $s = 3/4$ for 3D VRH [40] and 1 for 2D VRH [42]. In this picture, for the de-doped heterogeneous mixture of CNT junctions and CNT structures adding in series, the de-doped CNT junctions contribute to the VRH behavior while the de-doped metallic CNTs are not significantly contributing to MR. Best fits of VRH hoping models leads to a temperature-independent localization-length between 5 and 9 nm, which concurs with some CNT reports (4.6–9 nm [34,36,39,41]). However, the MR's temperature dependence does not have the predicted power-law form (Fig. 3d does not follow a power-law), nor do the most charitable fits for exponent s (0.25–0.27 for $T < T_M$ or 0.33–0.36 for all T) agree with the temperature power-law value in (equation (3)). Further, for VRH, MR should decrease going from transverse to longitudinal H orientations [97–99] (where field and electron-propagation are parallel, the resultant electron wave constriction does not hinder forward propagation); this decrease in longitudinal MR is not observed. While other mechanisms could be obfuscating the pure VRH response, our + MR also occurs near room-temperature, well above T_M where VRH no longer applies; both transverse and longitudinal + MR is present when there is a metallic-like $dR/dT > 0$ response.

Classical High-field + MR. A classical two-band model accounts for the curved trajectory of free-carriers from the Lorentz force and models the +MR response of graphite [100], carbon-fiber [101,102], and CNT materials [27,51] according to:

$$MR(\%) = 100\%\ \mu^2 H^2 \tag{4}$$

where μ is temperature-dependent electronic mobility, with equal numbers of holes and electrons, with equal μ, and with $\mu\ H \ll 1$. The cyclotron radius r_c can be calculated with conservative values [27] of effective mass m^* ($7.8\text{x}10^{-32}$ kg) and Fermi velocity v_f ($8\text{x}10^5$ m/s) according to $r_c = m^*\ v_f\ e^{-1} H^{-1}$, yielding r_c values 6.5 nm–39 nm for magnetic-fields 60 to 10 T, respectively, and is small enough to fit within CNT bundles. This opens the possibility that anisotropic CNT bundles could support two-band MR between junctions. More complicated classical two-band variations account for unbalanced carriers (with electron n_e and hole n_h carrier densities) and angle Θ between the graphitic-plane and H [101–103]:

$$MR(\%) = 100\% \frac{\frac{4 n_e n_h}{(n_e + n_h)^2} H^2\ Cos^2[\theta]}{\left(\frac{1}{\mu^2} + \left(\frac{n_e - n_h}{n_e + n_h}\right)^2 H^2\ Cos^2[\theta]\right)} \tag{5}$$

Here, the MR is initially quadratic with H, although saturates depending on hole/electron imbalances; as shown in (5), domination of one carrier leads to no MR (because the Hall voltage exactly balances the Lorentz force [104]) and this explains the lack of +MR in as-is CNT-conductors. Supporting this, Hall measurements on as-is (Supplemental-section 4.4) demonstrate holes are dominant with a relatively temperature-independent carrier-density. Alternatively, the +MR of de-doped CNT-conductors is quadratic without saturation, so it fits best to the simpler (equation (4)), supporting that electron/hole carrier densities are practically equal/compensated. Hall measurements for de-doped (Supplemental-section 4.4) had a Hall voltage that fit less reliably with field; further, the Hall sign would sporadically flip between hole and electrons, followed by a dramatic and consistent change to electron conduction over 300 K. A Hall sign change indicates competition between electron and hole conduction (weighted by mobility and number density). Similar results were observed with graphitic-intercalation-compounds, where the pristine graphite has large quadratic + MR (≈10^5 at 4.2 K and 2.3 T) [100], which can be partly [18,105] or fully [106,107] suppressed after doping.

Applying (4) on de-doped MR, fitted μ ranged from ≈20 to 110 cm^2/V s for 270 to 1.5 K respectively (Fig. 3d plots μ^2 versus T); this fitted μ is a composite mobility affected by both junctions, as well as CNT structures interactions. μ is on-par with unaligned CNT networks (2–200 cm^2/V s [57,106]) and direct-spun CNT fibers measured similarly (≈120–210 cm^2/V s [27]), though is well lower than the best individual CNTs (10,000 cm^2/V s [108]), graphitized carbon-fiber (≈7000 to 50,000 cm^2/V s [101]), and graphite (15,000 to 1,300,000 cm^2/V s [100]). Using our room-temperature μ from the transverse field (20 cm^2/V s) and typical SWCNT film carrier densities from literature (0.5–1.3 x10^{20} cm^{-3}) [109,110], this arrives at a conductivity of ≈0.04 MSm^{-1} and is closer to our de-doped ribbon conductivities measured perpendicular to the microstructure-alignment (0.01–0.02 MSm^{-1}). According to Matthiessen's rule, mobilities from different scattering mechanisms add in parallel: one mobility for elastic interaction (T independent) and, in parallel, another mobility for phonon interaction (T-power-law with exponent x). We get [27,101]:

$$\mu(T) = (\mu_{ELASTIC}^{-1} + \mu_{PHONON} T^{-x})^{-1} \tag{6}$$

Fits to this model (which are superior to our VRH fits) are shown in Fig. 3d with fitted x of 0.70. This x is greater than direct spun CNT fibers (x = 0.5) [27], although less than graphitized carbon-fiber [101] and individual CNTs [21,57,111–114] ($x = 1$, from thermal phonon scattering). Using MR for μ-characterization has proven useful for graphitized carbon-fiber where differences in graphitic perfection can no longer be resolved by Raman spectroscopy or X-ray diffraction [115]. Further, *quantitative* Hall measurements are difficult in heterogeneous systems like CNT films (as demonstrated by others [110] and us, Supplemental-sections 4.4 and 4.5), where the obscuration of the intrinsic Hall voltage amongst the heterogeneous conduction system over-estimates the carrier-density by several orders of magnitude.

Longitudinal High-field MR. Our de-doped CNT fibers also had significant *longitudinal* MR and, near room-temperature, this was greater than the transverse MR. While Lorentz force is zero with H parallel to current, classical two-band anisotropic semimetals can still have longitudinal MR from off-diagonals in the mobility matrix [116–118], notably such as graphite's large longitudinal MR when H and probe-current are normal the graphite plane (MR = 1200 % at 8 T and 4.2 K [119]). Beyond classical MR, another contender for longitudinal + MR can be bandgap modulation from the Aharonov-Bohm effect (discussed in the next section). It is likely both quantum and classical effects simultaneously contribute to longitudinal MR in varying degrees, which obfuscates longitudinal high-field analysis compared to the simpler transverse orientation.

It is interesting that both *transverse* two-band and VRH models predict similar characteristic lengths: distance between elastic scatter (4–4.7 nm, approximately calculated by $\mu_{ELASTIC}\ v_f\ m^*/e$) or VRH's localization length (5–9 nm). While our MR results largely favor classical two-band over VRH, independent of the selected mechanism, the quadratic + MR response in transverse high-field is correlated to improved conductivity of pristine CNT materials.

Angular MR. Our PPMS more precisely explored angle-dependent MR across a wider sample set by continuously rotating the sample in static field, albeit lower strength (≤9T). Starting with typical *transverse* MR, where the angle is fixed with low-field perpendicular to the sample, our results concur with literature [25,27,41,76,86,89]; that is, a -MR

that becomes more negative with lower temperature (for T < 10 K, MR: −1.5 - > −3 % (as-is) and −4 - > −6 % (de-doped), supplemental-Fig. 4.1-1–4). Then, just for de-doped below ≈5 K, a positive + MR component appears at higher field. Agreeing with multiple CNT studies [27,43,49,50,52,53,89], our -MR for all CNT-conductors (as-is/de-doped; ||/⊥ alignment; various aspect-ratios, Supplemental-section 4.2) fits best to 2D weak-localization with electron-electron dephasing; a somewhat worse fit is obtained from 1D weak-localization (used in InAs nanowires [120–123] and suggested for CNTs in Ref. [76]) and no significant fit with 3D weak-localization [25,49,54,124,125]. For all categories, our fitted 2D phase-coherence length ranges from ≈51 to 10 nm for temperatures 1.9–100 K respectively (supplemental-Fig. 4.2-1), similar to other CNT reports [27,89]. De-doped's closely-matching 2D weak-localization response was not expected; typically, -MR in VRH is from a conceptually similar interference mechanism for localized carriers, the so-called Sivan Entin-Wohlman Imry model (SEI) [40,126–128] used in multiple CNT studies [25,34–39,41,129]. Note that, because of the low-field + MR present in de-doped for $T \leq 5$ K, we only considered de-doped weak--localization when T ≥ 10 K (where + MR influence is assumed small). All-together, 2D weak-localization suggests charge carrier confinement. This confinement is possibly on CNT bundles surface [49]; conductive atomic force microscope (AFM) studies demonstrated thinner bundles are intrinsically more conductive than wider ones [58,60,61,113,130]. Alternatively, contiguous sheets of metallic CNTs embedded in the bundle, together with non-participating semi-conducting ones, also form a crumpled-sheet where 2D-confinement could apply. The distribution of current within a CNT bundle is explored in the tight-binding simulations in the next section. Supplemental-section 4.2 has the complete fitted weak-localization parameters and phase-coherence plots.

To now explore angle-dependent MR, which is less addressed in carbon-conductor literature (with exceptions [86,115]), we mechanically rotated the CNT-conductor orientation continuously in a steady DC magnetic-field H. Fig. 4a and supplemental-Fig. 4.3-3–4 shows MR modulation of a de-doped CNT fiber at 4.5 T: sweeping from angle 0° (H⊥CNT), through 90° (H||CNTs), all the way around to 360°. In this particular run, the probe-current is fixed to parallel the microstructure-alignment. Multiple temperatures are shown. At higher temperatures (≈60 K), MR at 0° (H⊥CNTs) starts negative and, moving away from 0°, plateaus to more negative MR, then repeats at 180°. At colder temperatures (≈3.5 K), a +MR component now develops approaching 90° (H||CNTs). With higher field (9 T, Fig. 4b), the +MR component at 90° now dominates across all temperatures. As-is has a similar response, although the MR modulation is smaller (MR <1.5 %, compared to de-dope's 6–20 %, supplemental-Fig. 4.3-5). Fourier analysis of the periodic traces (Supplemental-section 4.3-6) shows the 180° Fourier component is largest, corresponds to two-fold symmetry as expected from fiber morphology. 90° Fourier components are the next largest, corresponding to four-fold symmetry. Note that a constant and higher-order components are present, although are notably smaller. Supplemental-section 4.3.7–8 shows another angle-dependent MR with probe-current now perpendicular to the microstructure-alignment; the MR modulation is again similar to the original, supporting no intrinsic transport difference between with or against-the-grain.

Similar two and four-fold symmetry was also observed in the earlier angular-dependent MR study [86], which was attributed to significant residual iron catalyst; our case has only small traces of residual iron catalyst (supplemental-Fig. 1.3-1–2). Alternatively, classical two-band MR could contribute at low-field too; considering the greatest fitted high-field mobilities (1.5 K, transverse MR μ = 94–112 cm^2/Vs and longitudinal MR μ = 117 cm^2/Vs), this yielded MR ≈ 50 % at 60 T, although at 9 T this is an insignificant MR ≈ 1 %. Within weak-localization theory, with only inelastic dephasing (electron–electron/phonon) and no spin terms, MR is negative. When 3D, it is angle-independent. When 2D, it is most negative at 0° (H⊥confining-2D-plane) and MR should approach 0 % for 90° (H|| confining-2D-plane). Clearly, the angle-dependent MR differs from this simple weak-localization picture.

Due to CNT's cylindrical topology, their band-structure is sensitive to magnetic-flux threading the CNT diameter $\varphi = H\pi(d/2)^2$, with their 1D subbands shifting with field via the Aharonov-Bohm (AB) effect. This phenomenon is caused by coupling of the orbital motion to the magnetic-field, and is periodic with period $\varphi_0 = h/e$, where φ_0 is the flux quantum with Planck's constant h. In gapless CNTs at low-fields this response results in the gradual opening of a bandgap, and in initially gapped CNTs in its closing [96,131–133], which we propose as the main source of our -MR in parallel magnetic-field. The closing of semi-conducting bandgaps requires >100 T fields, but it is established that in metallic non-armchair CNTs the curvature of the atomic lattice opens a smaller bandgap, proportional to $\cos(3\vartheta)/d^2$ where ϑ is chiral angle [134]. This gap ranges from a few to a few tens of meV and is easily closed by experimentally available magnetic-fields. In Ref. [135], for example, an individual CNT (with small bandgap and $d = 1.5$ nm) is brought near the charge neutrality point with a gate-electrode and then subjected to pulsed, parallel-oriented 60 T magnetic-field. At 82 K, the conductance increases by 14 % from 0 to 5.9 T and, from there, the conductance plummets to ≈0 by 40 T. This modulation is a possible quantum contribution to our angle-dependent MR and classical longitudinal-MR in our high-field (hinted previously, Fig. 3c), and motivated the following effective model simulation.

Calculation of the orbital response in magnetic-field. The bandgap modulation via the Aharonov-Bohm mechanism is primarily caused by the coupling of the parallel component of the field to the orbital degree of freedom, which in CNTs corresponds to the valley, inherited from the CNTs parent graphene. This coupling has opposite sign for the K and K' valley, corresponding to clockwise and counter-clockwise motion of the electron around the CNTs perimeter. The spin in turn couples to the full magnetic-field through the Zeeman effect, but the orbital response is usually several times stronger. Model details are found in methods and Supplemental-section 5.1. The linear conductance through the infinite CNT with field-modulated band-structure is shown in Fig. 4c and d as a function of the field-orientation, with the dashed white lines marking the position of the band edges and the color background encoding the linear conductance smeared by the temperature at 3.5 K (other temperatures are explored in supplemental-Fig. 5.1-1–2). In this calculation the leads are formed by the left and right semi-infinite parts of the CNT, while the central part is finite. The bandgap varies periodically with a dominant 180° period, but it has also a weaker 90°-periodic component (more visible for $H_{||} = 4.5$ T). This subdominant component is caused by the fact that the gap closes at four positions: at $H_{||} = \pm H_{||,0}$ and at $H_{||} = \pm H_{||,0}$ +180°. At 4.5 T the gap closes near 45°, which leads to the apparent 90° periodicity. At $H = 9$ T the opened gap is so wide that $H_{||}$ reaches $H_{||,0}$ only close to 22°.

Slicing these data at $E_F = 0$ at different temperatures yields the MR of a single CNT in the de-doped state. Similar to our experimental angle-dependent MR, in Fig. 4e and f we see that at 4.5 T the MR at 0° is negative and decreasing with temperature; it features four dips spaced by ≈ 90° and flattens out towards higher temperatures. At 9 T the distinct + MR at 90° dominates the response. Other doping-levels are explored in supplemental-Fig. 5.1-3; this lowers the magnitude of the MR modulation, which was another experimental observation.

While the qualitative agreement between the experimental and theoretical result is quite good, there are some quantitative discrepancies. Firstly, the values for MR are unrealistically high. This is to be expected, since the calculation deals with a single CNT while the fiber is a composite of many CNTs with varying diameters and helicities, connected in parallel and in series – proper ensemble averaging would yield much lower MR magnitudes. Secondly, some features of the MR behave differently in the experiment and in theory. For instance, at $H = 4.5$ T the value of MR near 90° changes very little with temperature, but the theoretical result varies very strongly, to the point of the MR becoming positive at high temperatures. There again the collective nature of the

CNT fiber certainly comes into play, and with it likely weak-localization, missing in the single CNT calculation.

CNT Bundle Simulations. The CNT bundle is fundamental to the heterogeneous conductive network yet its distributed behavior is not fully understood. To investigate the electronic-transport distribution within a CNT bundle, with magnetic-field, we performed large-scale quantum transport calculations using tight-binding non-equilibrium Green's function (TB–NEGF) formalism. We modeled bundles composed of seven CNTs arranged in a flower-like, hexagonal configuration with the same or mixed helicity (either (9,9), (21,0), (12,3) or (20,0) or a mixture, see supplemental table 5.2-1 for geometry and selected transmission distribution). To match the experimental semi-conducting fraction (≈2/3), mixed bundles were carefully constructed with comparable composition and symmetry. We also modeled a large bundle of nineteen (9,9) CNTs arranged with hexagonal close-packed geometry, as well two CNT bundles separated by a junction (forcing inter-bundle tunnelling for conduction).

Our approach leverages TBtrans and the sisl Python library, both extended and customized for this work. To capture magneto-transport at high magnetic fields—where perturbative approaches break down—we implemented the Peierls substitution directly into both the Hamiltonian and the overlap matrices across the entire system, including electrodes. This modification allows a fully gauge-consistent treatment of external magnetic-fields up to 60 T, oriented perpendicular to the CNT bundle (Supplemental Table 5.2-1, Supplementary Figure 5.2-4). Importantly, all systems span more than 10 nm in length and contain thousands of atoms, making this study among the first to achieve such transport simulations at this scale and level of theory, while retaining full

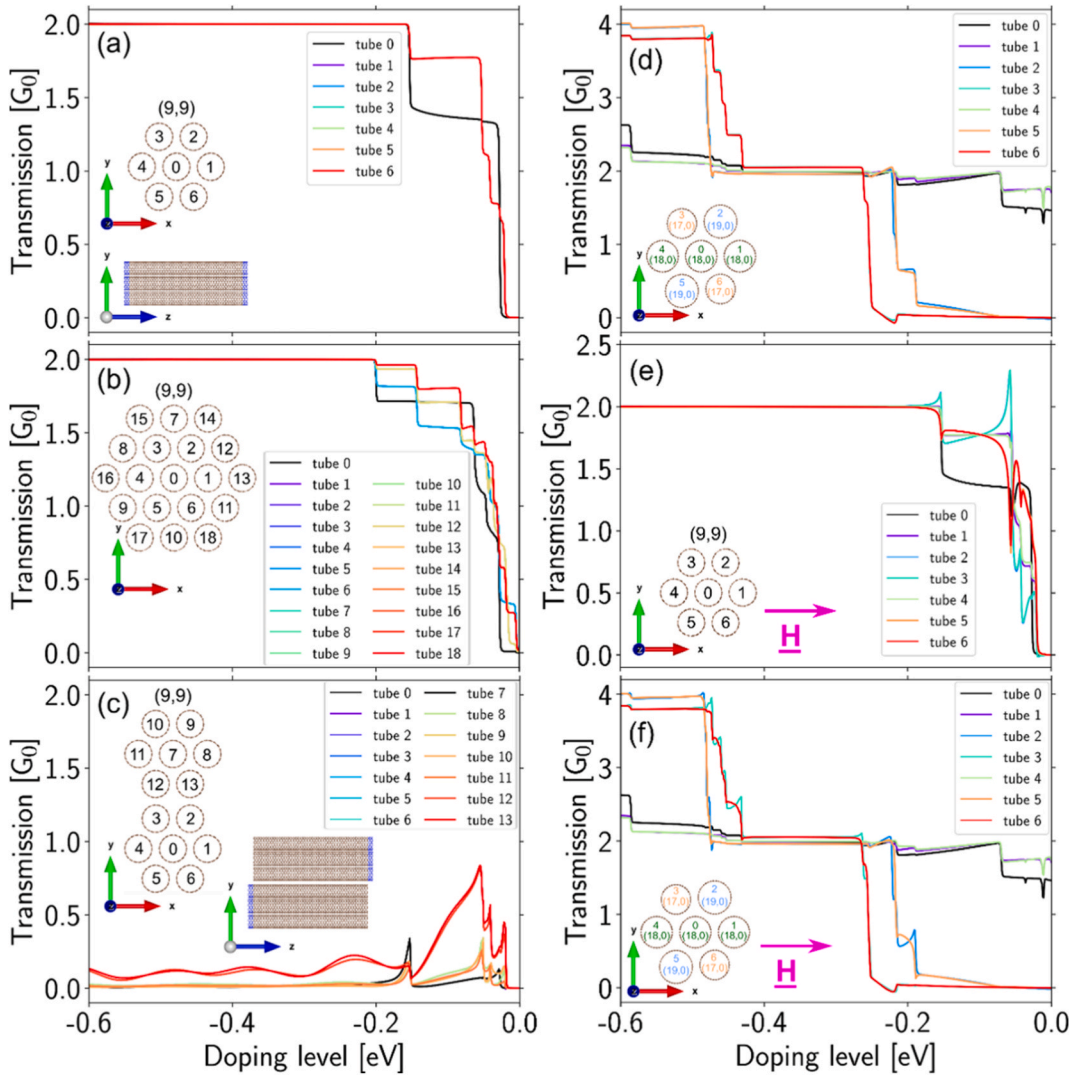

Fig. 5. CNT-resolved, individualized transmission for various CNT bundles versus doping level; the insets show side and cross-sectional views of the hexagonal CNT bundle arrangement where all CNTs are connected to semi-infinite electrodes (blue). a, Metallic bundle composed of seven (9,9) CNTs at $H = 0$ T; due to the symmetry CNTs 1, 2, 3, 4, 5, and 6 have the same transmission (red line). b, Larger metallic-bundle composed of nineteen (9,9) CNTs at $H = 0$ T; inset shows a central CNT is surrounded by six in a middle layer and twelve in an outer layer, forming a finite hexagonal close-packed (HCP) arrangement; due to the symmetry, the transmission is the same for CNTs 1, 2, 3, 4, 5, and 6 (blue line), CNTs 7, 8, 9, 10, 11, and 12 (yellow line) and CNTs 13, 14, 15, 16, 17, and 18 (red line). c, Junction composed of two metallic bundles of seven (9,9) CNTs each at $H = 0$ T; the inset demonstrates how electron tunnelling between bundles is required for conduction; due to the symmetry, the transmission is the same for CNTs 0 and 7 (black line), 1 and 11 (dark-orange line), 2 and 12 (light-red line), 3 and 13 (dark-red line), 4 and 8 (green line), 5 and 9 (yellow line), and 6 and 10 (light-orange line). d, Mixed bundle consisting of three metallic (18,0) CNTs (CNTs: 0, 1, and 4), two semiconducting (19,0) CNTs (CNTs: 2 and 5), and two semiconducting (17,0) CNTs (CNTs: 3 and 6) at $H = 0$ T. e, Metallic (9,9) CNT bundle with $H = 9$ T perpendicular to the bundle (along the x-axis, as indicated). f, Mixed CNT bundle with $H = 9$ T perpendicular to the bundle (along the x-axis as indicated). Semiconducting CNTs are labeled with lighter-colored numbers and metallic with darker-colored numbers. CNTs are plotted to scale, so differences in cross-sectional size reflect actual diameter variations. (For interpretation of the references to color in this figure legend, the reader is referred to the Web version of this article.)

quantum coherence.

We first consider individual CNT bundles composed of all-metallic, identical CNTs with each CNT end uniformly connected to electrodes, without magnetic-field. When evaluated near the Fermi level $E_f = 0$ (un-doped), the transmission is frequently lower in the bundle core; this is shown in a seven-armchair bundle (Fig. 5a), particularly very close to Fermi level $E_f = 0$ at the pseudo-gap formed by armchair interaction (5.6 % core vs 15.7 % outer, supplemental table 5.2-1). Lower core transmission is also for the seven-(12,3) bundle (0.33 % core vs 16.5 % outer, supplemental table 5.2-1). Near-zero transmission is also present in the center CNT of an un-doped, large 19-armchair bundle (0.25 % core vs 3–7 % outer, Fig. 5b and supplemental table 5.2-1). Structural relaxation of the bundle slightly deforms the central CNT from circular to off-circular, but largely does not alter the overall transmission profile. This demonstrates that our primary conclusions, even if drawn from mostly unrelaxed systems, remain valid and physically meaningful.

There are exceptions to lower core transmission in de-doped CNTs. A de-doped seven-(21,0) bundle has instead near uniform bundle transmission (supplemental table 5.2-1). This was a relatively large diameter and, in this isolated case, incorporating relaxation resulted in return to lower core transmission (6.5 % core vs 15.5 % outer, supplemental table 5.2-1 and Figs. 5.2–2). Further, when in a seven-(9,9)-armchair bundle, the center CNT was individually axially rotated by 20° (Supplemental-Fig. 5.2-2–3), the transmission through the rotated central CNT greatly exceeded the outer CNTs at $E_f = 0$ (75.3 % core vs 4.1 % outer). However, geometry optimization reveals that this rotated configuration is energetically less favorable (Supplemental Table 5.2-2), suggesting that the outer-conducting configuration is more likely in realistic conditions. For the large 19-armchair bundle, while the central CNT has near-zero de-doped transmission (0.25 %), the adjacent CNT middle layer carries a larger de-doped transmission density (7.2 %) than the surface layer CNT (3.3–6.2 %). Critically however, after even small doping (>0.1 eV), the transmission across any metallic-bundle becomes near uniform and overall greatly increases; the doped bundle conductivity converges to the sum of ballistic metallic CNT conductivity (each contributing two $G_0 = 4e^2/h$) or greater (for seven-(21,0) bundle, 50 % greater from sub-band doping). This underscores doping's importance, even for all-metallic CNT bundles.

Now consider bundles with semi-conducting CNTs. For un-doped bundles of mixed metallicities, metal CNTs carry the transmission at $E_f = 0$. For a mixed seven-CNT bundle with three (18,0) metallic CNTs in a row (Fig. 5d), the bundle transport is concentrated across the metallic CNTs with less transmission in the middle (29.89 % core vs 34.88 % and 35.63 % for outer metallic CNTs). Although the outer values are not identical, due to local atomic arrangements and inter-tube interactions, the trend remains: outer CNTs have higher transmission. Exploring this further, we simulated a 7-mixed bundle composed of two outer and opposing metallic CNTs with five interchangeable semi-conducting CNTs (Supplementary Figure 5.2-1). These semi-conducting CNTs were composed of two different semi-conducting helicities ((19,0) and (20,0)), where their bundle position was swapped without changing composition. In the de-doped case, the metallic CNTs always dominated the transport as expected, although metallic CNT-4 had a lion's share of the metallic transmission over metallic CNT-1 due to the inter-tube interactions. Swapping the positions of the semi-conducting helicities did quantitatively change the overall bundle transmission and somewhat modify the transmission partitioning across the metallic CNTs; qualitatively however, CNT-4 still captured most of the transport independent of adjacent semi-conducting helicities. This swapping observation, along with our other core bundle results, supports our previous case of the mixed bundle where transmission is less in the middle metallic CNT; therefore, the lower core transmission is better explained by its central location opposed to interaction from particular adjacent semiconducting CNTs. A de-doped fully semi-conducting seven-(20,0) bundle (Supplementary Figure 5.2-3d), due to its bandgap, exhibits zero transmission and the first non-zero contributions appear only at higher energies. As such, the CNT-resolved transmission profile at low energies is not directly representative of conducting behavior and should not be interpreted in the same way as metallic systems. Contrasting all-metallic-bundles, greater doping (0.6 eV) is required to make uniform non-zero transmission. Once activated however, the mixed or all-semi-conducting bundles (supplemental table 5.2-1) can have transmission greater than the equivalent doped metallic bundle of similar diameter (compare the results for a seven-(21,0) versus seven-(20,0) zigzag bundles); this illustrates that sufficiently doped semi-conducting CNTs can be better conductors then metallic CNTs, doped or un-doped.

Now consider two parallel seven-armchair CNT bundles separated by a junction; the bundles' far-ends uniformly connect to electrodes and the bundles' close-ends overlap (10.33 nm overlap with 0.34 nm separation, Fig. 5c), forcing transmission across the junction. Despite uniform electrode connection, and independent of the doping level, only CNTs directly adjacent to the other bundle participate in conduction (four out of 14, Fig. 5c). This is the only studied situation resulting in low bundle cross-section utilization, independent of doping-level. This key result implies that, for real-world CNT fibers with bundle junctions, thinner CNT bundles always have greater cross-sectional utilization.

Next, magnetic-field is considered for CNT bundle transport. Fig. 5e and f shows transmission under a 9 T perpendicular field for a metallic (9,9) bundle and a mixed bundle, respectively. A direct comparison with the zero-field configurations (Fig. 5a and d) reveals the spatial transmission distribution remains largely unchanged from field. In Fig. 5e and Supplementary Figures 5.2-4 a–c however, we observe spikes in the individual transmission curves for outer tubes when field is applied, particularly within the energy range −0.2 eV to 0 eV. These spikes highlight the sensitivity of coherent transport in metallic systems to magnetic phase effects and inter-tube interference. Despite these local doping spikes for individual CNTs, the overall bundle transmission is not significantly modulated for perpendicular magnetic-field (from 4.5 to 60 T), the seven-armchair or mixed bundle cases, across the doping energy continuum (supplemental table 5.2-1, Figs. 5.2–4).

4. Discussion

Heterogeneous FIT has long been proposed [56] for CNT-conductors, although is often overlooked in authoritative CNT transport papers [25], and here we uniquely show its unavoidable relevance with the semi-conducting-like temperature response leveling-off to a constant value approaching absolute-zero. Further support includes 1) the well-established mixed metallic-like and semi-conducting-like temperature responses; 2) the dependence of cryogenic-resistance-ratio on CNT length, which is longer than any homogeneous characteristic length; and 3) Drude conduction signatures with high-field MR and Hall measurements. Homogeneous mechanisms still, however, contribute: 1) weak-localization causes transverse -MR and 2) de-doping leads to VRH. Further, considering the conductivity anisotropy does not change significantly temperature implies that: 1) the anisotropy is created by the extrinsic difference in path lengths between "with-grain" and "against-the-grain"; 2) that current distribution across the various network paths does not change much with temperature. 3) Thus, a simple series sum of CNT structure and junction resistances are sufficient for network modeling and tributary pathways that open up at higher temperature, while present to some degree, are not overall significant. Similar extrinsic network geometry narratives [81,136] and simple resistance series sums [24,27,37,55,65] have been found in other CNT materials.

What are the consequences of accepting a heterogeneous system where resistance components simply sum in series? At sufficiently warm temperatures, both VRH and FIT become Arrhenius style thermal-activation $R_{SemiCond}(T) = R_c\, exp\left(\frac{K}{T}\right)$ with fitting factors R_c and K. This Arrhenius region may be identified as a straight segment on an Arrhenius plot ($\ln R$ vs T^{-1}) before the upswing from metallic resistance. Using

the heterogeneous model $R(T) = R_{SemiCond}(T) + R_{Metal}(T)$ and just considering the warmer region where Arrhenius style thermal-activation applies, the semi-conducting contribution may be subtracted-out after fitting. This leaves the intrinsic metallic resistance without specifying the semi-conducting form and is shown in Fig. 6 below. Fig. 6a shows the relative metallic contribution to the total resistance at room-temperature $\left(100\% \frac{R_{Metal}(300K)}{R(300K)}\right)$ versus aspect-ratio. For as-is with parallel microstructure-alignment, this relative metallic contribution (≈16–55 %) increases almost linearly with aspect-ratio (power-law 0.85 ±0.11), because junctions take less share of network resistance with longer CNTs; extrapolating, 100 % metallic conduction requires an aspect-ratio of at least ≈12000. De-doped have lower metallic fractions (≈4–12 %) without correlation to aspect-ratio, because junctions here dominate network resistance independent of CNT length. Cross-grain samples have similar metallic fractions and correlations as their counterparts, despite a ≈20x difference in conductivity; its network path has the same junction/structure relationship as for the parallel-alignment, although the cumulative network path is meandering and much longer (in this framework, 20x longer).

Fig. 6b shows the room-temperature, metallic component specific-conductivity of as-is and de-doped CNT-conductors if extrinsic junctions were eliminated, compared against relevant benchmarks. This calculation assumes that the network path length is minimized; for parallel microstructure-alignment this is approximately true, while perpendicular are not considered here. As shown, metallic component specific-conductivity are well above copper and some as-is fibers are

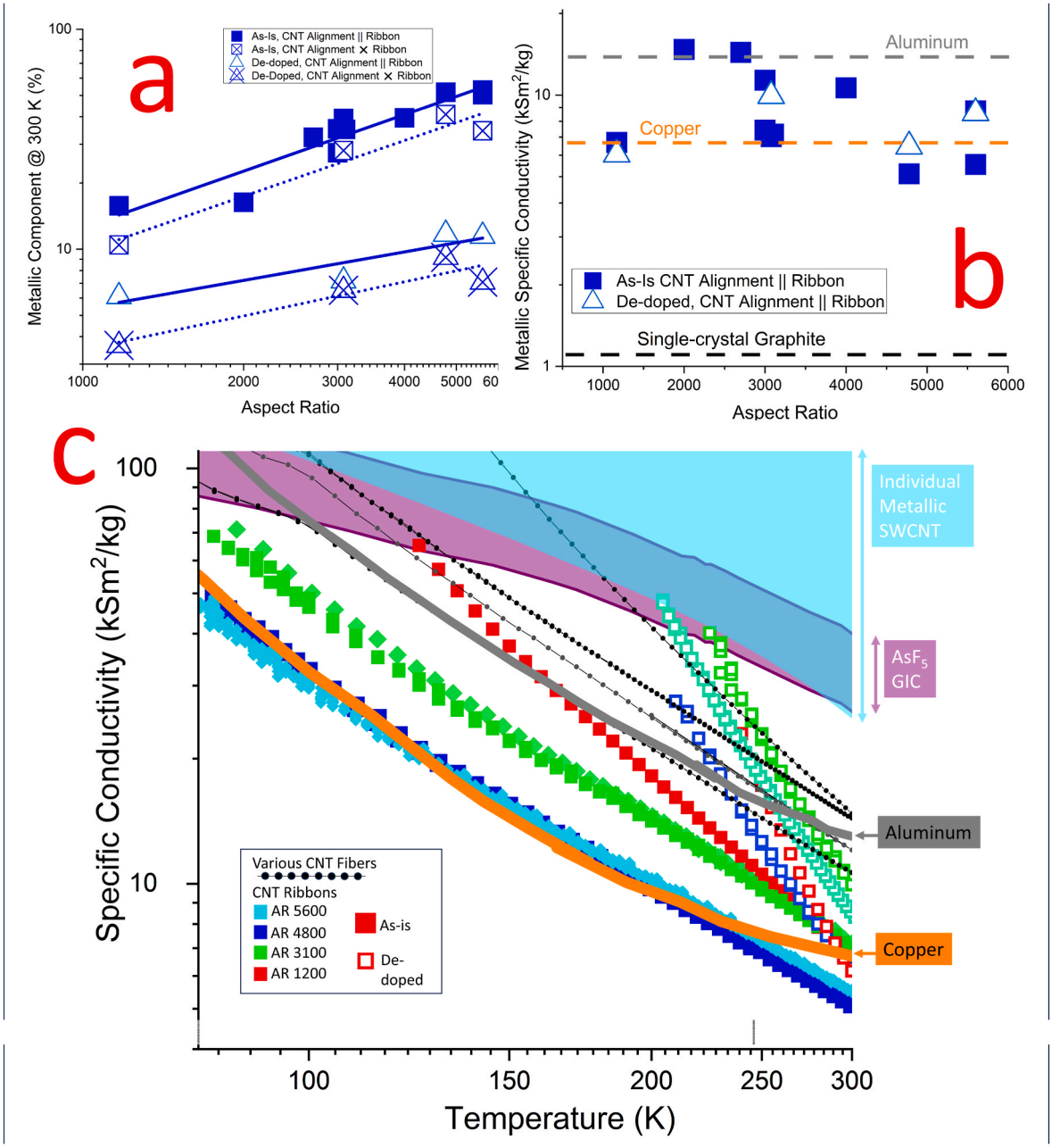

Fig. 6. Estimating metallic component conductivity. Subtracting the fitted component of Arrhenius thermal-activation leaves the metallic component with relatively few assumptions on transport mechanisms. a, aspect-ratio (AR) versus the metallic percentage of total room-temperature resistance. b, The room-temperature specific-conductivity of the metallic component compared to copper and aluminum. c, temperature-dependent specific-conductivity of metallic components with different aspect-ratios (AR) and doping status, alongside relevant benchmarks [137,138].

above aluminum (the highest practical specific-conductivity metal). There is no correlation with aspect-ratio, reflecting its intrinsic nature. The metallic component specific-conductivity of de-doped and as-is are comparable at room-temperature. Conductive AFM studies on sparse CNT networks show that doping both enhances transmission across junctions as well as increases carrier-density [61,139], contrasting graphitic-intercalation-compounds (GICs) where doping just increases carrier-density [18]. In our case, the doping-enhanced carrier-density and improved junction transmission may be partially countered by increased scattering within bundles. Fig. 6c shows the temperature-dependence of the metallic component specific-conductivity with different aspect-ratio and doping-status. Other advanced carbon conductors (GICs, individual metal CNTs) and metal benchmarks (copper, aluminum) are shown based on their reported resistance vs temperature plots and room-temperature specific--conductivity. As-is is between copper and aluminum. De-doped traces have a steeper temperature-dependence, likely from a decrease in the proposed doping induced scattering.

In conclusion, the quantitative understanding and controlling of the semi-conducting-like and metallic like conductivity responses to temperature is practical and necessary for overall conductivity improvement. Were it not for the junctions, the conductivity of CNT-conductors already exceeds copper and aluminum. For both as-is and de-doped, increasing aspect-ratio decreases the junctions' impact; a 12000 aspect-ratio should then lead to significant junction suppression at room-temperature. Increasing aspect ratio further will have diminishing returns at room-temperature, although could lead to a completely metallic-like conductivity response down to liquid-helium temperatures ($d\sigma/dT < 0$ for all T). From that point, continued conductivity improvement is now reliant on improving the intrinsic metallic structure (thinner bundles, less defects, and optimally doped semi-conducting CNTs). Fully de-doped CNT-conductor electrons become localized at cryogenic temperatures, despite the relatively favorable degree of microstructure-alignment, graphitic quality, and aspect-ratio. This contrasts the behavior of their older analog single-crystal graphite which already has the full metallic-like temperature response. A fundamental difference is that single-crystal graphite has planes in registry and this order does not easily exist for CNTs within a bundle; further, fully de-doped semi-conducting CNTs are simply deadweight. Notably large tight-binding calculations showed complex current distributions within a de-doped bundle, where transmission tended to be lower in the core of metallic CNTs; doping universally increased the uniformity and overall transmission of bundles of mixed, fully-semi-conducting, and fully-metallic CNT composition. Critically, they demonstrated that when one bundle is connected to another in series, only the CNTs adjacent to the other bundle participate in the transport, independent of the doping-level. This favors thinner bundles with more connections for higher conductivity. The impact of the perpendicular magnetic field in on transmission distribution within a bundle is small.

The low-field negative MR across all samples best follows 2D weak-localization; we conclude that the main components of the network are not individual CNTs but their bundles, and that bundle transport is at least partially coherent. As found by others, the 2D character hints that the transport occurs either at the bundle surface or in contiguous crumpled-sheets of metallic CNTs embedded in the bundle. The magnetic-field orientation study, including substantial longitudinal MR near room-temperature, indicates that the transport response carries a strong signature due to the individual components, in the form of the gap modulation via the Aharonov-Bohm effect due to the parallel component of the field. We found that the positive quadratic MR at high-field for de-doped CNT materials is governed by a characteristic parameter related to higher conductivity, likely classical in nature. As conductivity and the characteristic length increases, this + MR signal will become more accessible at lower field; this is particularly useful as Raman and X-Ray diffraction lose resolution for highly graphitic systems and Hall measurements are less effective for heterogeneous systems. Recent advances [1–10,14–17] in CNT-conductor conductivity are encouraging and could reach the level of the best graphitic intercalated compounds (50 % greater than copper), although stronger and bendable. Understanding and controlling their temperature and magnetic field-dependent electronic transport will aid in this development. The socio-economic impact of copper-to-carbon replacement in wires would be transformational [140–144], encouraging movement away from copper supply chains and movement towards carbon-capture [145], allowing light-weight and sag-free power transmission-cables [141,146,147], high-performance all-carbon electric machines [140,143,148], and electricity delivery in demanding aerospace [141,144,149], high-radiation [150], and chemically harsh [151,152] environments.

CRediT authorship contribution statement

John Bulmer: Writing – original draft, Methodology, Investigation, Formal analysis, Conceptualization. **Chris Kovacs:** Resources, Methodology, Investigation. **Thomas Bullard:** Software, Formal analysis, Data curation. **Charlie Ebbing:** Resources, Investigation. **Timothy Haugan:** Supervision, Resources, Project administration. **Ganesh Pokharel:** Resources, Methodology, Investigation. **Stephen D. Wilson:** Supervision, Resources. **Fedor F. Balakirev:** Supervision, Resources, Methodology, Investigation. **Oscar A. Valenzuela:** Resources, Methodology, Investigation. **Michael A. Susner:** Resources, Methodology, Investigation. **David Turner:** Resources, Investigation. **Pengyu Fu:** Resources, Conceptualization. **Teresa Kulka:** Writing – original draft, Methodology, Investigation, Data curation. **Jacek Majewski:** Writing – review & editing, Supervision. **Irina Lebedeva:** Software, Resources. **Karolina Z. Milowska:** Writing – review & editing, Supervision, Methodology, Investigation. **Agnieszka Lekawa-Raus:** Resources, Investigation, Conceptualization. **Magdalena Marganska:** Writing – review & editing, Validation, Methodology, Investigation, Formal analysis.

Declaration of competing interest

The authors declare that they have no known competing financial interests or personal relationships that could have appeared to influence the work reported in this paper.

Acknowledgements

This work was performed at the National High Magnetic Field Laboratory and is supported by the National Science Foundation, the Department of Energy, and the State of Florida through NSF Cooperative Grant No. DMR-1157490 and by U.S. DOE BES Science at 100 T project. Some of this work was supported by the Air Force Office of Scientific Research (LRIR #18RQCOR100 and #24RQCOR004). This research was performed while J.B. held an NRC Research Associateship award at the U.S. Air Force Research Laboratory (AFRL), Aerospace System Directorate (AFRL/RQ). We wish to thank the Carbon Hub and Dexmat for material support. SDW and GP gratefully acknowledge support via the UC Santa Barbara NSF Quantum Foundry funded via the Q-AMASE-i program under award DMR-1906325. Special thank you to Rober Waelder (AFRL) and Matthew Foster, Geoff Wehmeyer, Junichiro Kono (Rice University) and Vasili Perebeinos (University of Buffalo) for valuable discussions on carbon nanotube transport.

T.K. and K.Z.M. gratefully acknowledge the Interdisciplinary Centre for Mathematical and Computational Modelling at University of Warsaw, Poland (Grant No. G47-5) for providing computer facilities and technical support. T.K. and I.L. also acknowledge the technical and human support provided by the DIPC Supercomputing Center, Spain. T. K., K.Z.M. and I.L. are grateful to the Agencia Estatal de Investigación, Ministerio de Ciencia e Innovación, Spain for funding this research under Proyectos de Generación de Conocimiento 2022 program, PID2022-139776NB-C65. K.Z.M also would like to thank the European

Commission (Marie Skłodowska-Curie Cofund Programme; grant no. H2020-MSCA-COFUND-2020-101034228-WOLFRAM2) for supporting this research. T.K. acknowledges the 3rd edition of Microgrants in Action IV.4.1 - 'A complex programme of support for UW PhD students', implemented as part of the 'Excellence Initiative - Research University' (IDUB) Programme. JAM acknowledges the support from Centera2 project (FENG.02.02-IP.02.01-IP.05-T0004/23) funded with IRA FENG program of Foundation for Polish Science, and co-financed by the EU FENG Programme. A.L.-R. would like to thank Warsaw University of Technology, Poland—Excellence Initiative (Materials Technologies–3 ADVANCED, grant agreement no 1820/359/Z01/POB5/2021) for funding this research. M.M. gratefully acknowledges helpful discussions with Leonid Golub.

Appendix A. Supplementary data

Supplementary data to this article can be found online at https://doi.org/10.1016/j.carbon.2025.121162.

References

[1] L.W. Taylor, et al., Improved properties, increased production, and the path to broad adoption of carbon nanotube fibers, Carbon N Y 171 (2021) 689–694.
[2] S. Xue, et al., Electrical and mechanical properties of high electrical conductivity CNT/Cu-yarns with Br doping and Cu encapsulation, Nano. Select 3 (2022) 129–139.
[3] D. Lee, et al., Highly conductive and mechanically strong metal-free carbon nanotube composite fibers with self-doped polyaniline, Carbon N Y 213 (2023) 118308.
[4] S.G. Kim, et al., Hierarchical structure control in solution spinning for strong and multifunctional carbon nanotube fibers, Carbon N Y 196 (2022) 59–69.
[5] H.-Z. Wang, et al., FeCl3-Filled double-wall carbon nanotube fibers with record-high ampacity and conductivity, Adv. Fiber Mater. (2025), https://doi.org/10.1007/s42765-025-00623-9, 10.1007/s42765-025-00623-9.
[6] S. Hong, et al., Carbon nanotube fibers with high specific electrical conductivity: synergistic effect of heteroatom doping and densification, Carbon N Y 184 (2021) 207–213.
[7] S. Jo, A. Mikhalchan, S. Hong, S. Kim, S.G. Kim, S.M. Kim, D.-Y. Kim, B.-C. Ku, J. J. Vilatela, J.Y. Hwang, Highly conductive hybrid carbon nanotube fibers: Strategies and future directions for replacing copper with next-generation conductors, Compos. Part B: Eng. 300 (2025) 112471.
[8] L. Piraux, F. Araujo, T. Bui, M. Otto, J. Issi, Two-dimensional quantum transport in highly conductive carbon nanotube fibers, Phys. Rev. B Condens. Matter 92 (2015) 085428.
[9] H.-Z. Wang, X.-Y. Jiao, Z.-Q. Gao, P.-X. Hou, Highly conductive double-wall carbon nanotube fibers produced by dry-jet wet spinning, Adv. Funct. Mater. 34 (2024) 2404538.
[10] Y. Liu, M. Yang, K. Pang, F. Wang, Z. Xu, W. Gao, C. Gao, Environmentally stable macroscopic graphene films with specific electrical conductivity exceeding metals, Carbon 156 (2020) 205–211.
[11] D.S. Lee, et al., Ultrahigh strength, modulus, and conductivity of graphitic fibers by macromolecular coalescence, Sci. Adv. 8 (2022).
[12] Y. Niu, et al., Continuous carbon nanotube fiber with an extremely high average specific strength of 4.1 N·tex−1, Nano Res. 18 (2025) 94907584.
[13] X. Zhang, et al., Carbon nanotube fibers with dynamic strength up to 14 GPa, Science (1979) 384 (2024) 1318–1323.
[14] D.E. Tsentalovich, et al., Influence of carbon nanotube characteristics on macroscopic fiber properties, ACS Appl. Mater. Interfaces 9 (2017) 36189–36198.
[15] John S. Bulmer, A. Kaniyoor, J.A. Elliott, A meta-analysis of conductive and strong carbon nanotube materials, Adv. Mater. 33 (2021) 2008432.
[16] C.Y. Sun, et al., Ultrathin carbon nanotube fibers with a record high ampacity fabricated using a water coagulation Bath, Adv. Funct. Mater. (2025), https://doi.org/10.1002/adfm.202518867, 10.1002/adfm.202518867.
[17] C. Madrona, et al., Continous intercalation compound fibers of bromine wires and aligned CNTs for high-performance conductors, Carbon N Y 11 (2022) 133–143.
[18] M.S. Dresselhaus, G. Dresselhaus, Intercalation compounds of graphite, Adv. Phys. 30 (1981) 139–326.
[19] J. Shioya, Y. Yamaguchi, H. Matsubara, S. Murakami, Properties of AsF5-Intercalated vapor grown graphite, in: Properties of AsF5-Intercalated Vapor Grown Graphite 1986, 1986, pp. 238–243.
[20] H. Matsubara, Y. Yamaguchi, J. Shioya, S. Murakami, Preparation and properties of graphite grown in vapor phase, Synth. Met. 18 (1987) 503–507.
[21] M.S. Purewal, et al., Scaling of resistance and electron mean free path of single-walled carbon nanotubes, Phys. Rev. Lett. 98 (2007) 1868082.
[22] J.E. Fischer, et al., Metallic resistivity in crystalline ropes of single-wall carbon nanotubes, Phys. Rev. B Condens. Matter 55 (1997) R4921–R4924.
[23] A.B. Kaiser, V. Skákalová, Electronic conduction in polymers, carbon nanotubes and graphene, Chem. Soc. Rev. 40 (2011) 3786–3801.
[24] J. Bulmer, et al., Photonic sorting of aligned, crystalline carbon nanotube textiles, Sci. Rep. 7 (2017) 12977.
[25] J. Vavro, J.M. Kikkawa, J.E. Fischer, Metal-insulator transition in doped single-wall carbon nanotubes, Phys. Rev. B Condens. Matter 71 (2005) 155410.
[26] N. Behabtu, et al., Strong, light, multifunctional fibers of carbon nanotubes with ultrahigh conductivity, Science (1979) 339 (2013) 183.
[27] J. Bulmer, A. Lekawa-Raus, D. Rickel, F. Balakirev, K. Koziol, Extreme magneto-transport of bulk carbon nanotubes in sorted electronic concentrations and aligned high performance fiber, Sci. Rep. 7 (2017) 12193.
[28] C.A. Klein, Pyrolytic graphites: their description as semimetallic molecular solids, J. Appl. Phys. 33 (1962) 3338–3357.
[29] L.J. Collier, W.S. Stiles, W.G.A. Taylor, The variation with temperature of the electrical resistance of carbon and graphite between 0° C and 900° C, Proc. Phys. Soc. 51 (1939) 147–157.
[30] A.B. Kaiser, Metallic behaviour in highly conducting polymers, Synth. Met. 45 (1991) 183–196.
[31] J. Tsukamoto, Recent advances in highly conductive polyacetylene, Adv. Phys. 41 (1992) 509–546.
[32] K. Lee, et al., Metallic transport in polyaniline, Nature 441 (2006) 65–68.
[33] R. Friend, Polymers show they're metal, Nature 441 (2006) 37.
[34] M. Jaiswal, W. Wang, K. Fernando, Y. Sun, R. Menon, Charge transport in transparent single-wall carbon nanotube networks, J. Phys. Condens. Matter 19 (2007) 446006.
[35] M. Fuhrer, et al., Nonlinear transport and localization in single-walled carbon nanotubes, Synth. Met. 103 (1999) 2529–2532.
[36] M. Salvato, et al., Low temperature conductivity of carbon nanotube aggregates, J. Phys. Condens. Matter 23 (2011) 475302.
[37] V.K. Ksenevich, et al., Localization and nonlinear transport in single walled carbon nanotube fibers, J. Appl. Phys. 104 (2008) 073724.
[38] Y. Yosida, I. Oguro, Variable range hopping conduction in bulk samples composed of single-walled carbon nanotubes, J. Appl. Phys. 86 (1999) 999–1003.
[39] M. Jaiswal, W. Wang, K.A.S. Fernando, Y.P. Sun, R. Menon, Magnetotransport in transparent single-wall carbon nanotube networks, Phys. Rev. B Condens. Matter 76 (2007) 113401.
[40] R. Rosenbaum, T. Murphy, E. Palm, S. Hannahs, B. Brandt, Magnetoresistance of insulating amorphous NixSi1-x films exhibiting mott variable-range hopping laws, Phys. Rev. B Condens. Matter 63 (2001) 094426.
[41] M. Salvato, et al., Effect of potassium doping on electrical properties of carbon nanotube fibers, Phys. Rev. B Condens. Matter 84 (2011) 233406.
[42] T. Takano, T. Takenobu, Y. Iwasa, Enhancement of carrier hopping by doping in single walled carbon nanotube films, J. Phys. Soc. Japan 77 (2008) 124709.
[43] K. Yanagi, et al., Transport mechanisms in metallic and semiconducting single-wall carbon nanotube networks, ACS Nano 4 (2010) 4027–4032.
[44] G. Bergmann, Weak localization in thin films. a time-of-flight experiment with conduction electrons, Phys. Rep. 107 (1984) 1–58.
[45] V. Bayot, L. Piraux, J. Michenaud, J. Issi, Weak localization in pregraphitic carbon fibers, Phys. Rev. B 40 (1989) 3514–3523.
[46] P.A. Lee, T.V. Ramakrishnan, Disordered electronic systems, Rev. Mod. Phys. 57 (1985) 287–337.
[47] V. Bayot, et al., Two-dimensional weak localization in partially graphitic carbons, Phys. Rev. B 41 (1990) 11770–11779.
[48] L. Pirauxa, Weak localization and coulomb interaction in graphite intercalation compounds and related materials, J. Mater. Res. 5 (1990) 1285–1298.
[49] M. Salvato, et al., Weak localization and dimensional crossover in carbon nanotube systems, Eur. Phys. J. B 85 (2012) 109.
[50] J.Z. Cai, et al., Pressure-induced transition in magnetoresistance of single-walled carbon nanotubes, Phys. Rev. Lett. 97 (2006) 026402.
[51] S.N. Song, X.K. Wang, R.P.H. Chang, J.B. Ketterson, Electronic properties of graphite nanotubes from galvanomagnetic effects, Phys. Rev. Lett. 72 (1994) 697–700.
[52] G. McIntosh, et al., Orientation dependence of magneto-resistance behaviour in a carbon nanotube rope, Thin Solid Films 417 (2002) 67–71.
[53] L. Langer, et al., Quantum transport in a multiwalled carbon nanotube, Phys. Rev. Lett. 76 (1996) 479–482.
[54] P. Choudhury, M. Jaiswal, R. Menon, Magneto conductance in single-wall carbon nanotubes: electron-electron interaction and weak localization contributions, Phys. Rev. B Condens. Matter 76 (2007) 235432.
[55] R. Bhatia, V. Prasad, R. Menon, Probing the inter-tube transport in aligned and random multiwall carbon nanotubes, J. Appl. Phys. 109 (2011) 053713.
[56] A.B. Kaiser, G. Düsberg, S. Roth, Heterogeneous model for conduction in carbon nanotubes, Phys. Rev. B 57 (1998) 1418–1421.
[57] N.F. Zorn, J. Zaumseil, Charge transport in semiconducting carbon nanotube networks, Appl. Phys. Rev. 8 (2021) 041318.
[58] K. Mustonen, et al., Uncovering the ultimate performance of single-walled carbon nanotube films as transparent conductors, Appl. Phys. Lett. 107 (2015) 143113.
[59] C. Gabbett, et al., Understanding how junction resistances impact the conduction mechanism in nano-networks, Nat. Commun. 15 (2024) 4517.
[60] P.E. Lyons, et al., The relationship between network morphology and conductivity in nanotube films, J. Appl. Phys. 104 (2008) 044302.
[61] P.N. Nirmalraj, P.E. Lyons, S. De, J.N. Coleman, J.J. Boland, Electrical connectivity in single-walled carbon nanotube networks, Nano Lett. 9 (2009) 3890–3895.
[62] D. Adinehloo, W. Gao, A. Mojibpour, J. Kono, V. Perebeinos, Phonon-assisted intertube electronic transport in an armchair carbon nanotube film, Phys. Rev. Lett. 130 (2023) 176303.
[63] P. Sheng, Fluctuation-induced tunneling conduction in disordered materials, Phys. Rev. B 21 (1980) 2180–2195.

[64] A.B. Kaiser, Metallic behavior in highly conducting polymers, Synth. Met. 45 (1991) 183–196.
[65] A.B. Kaiser, V. Skákalová, S. Roth, Modelling conduction in carbon nanotube networks with different thickness, chemical treatment and irradiation, Phys. E Low Dimens. Syst. Nanostruct. 40 (2008) 2311–2318.
[66] Y.H. Lin, S.P. Chiu, J.J. Lin, Thermal fluctuation-induced tunneling conduction through metal nanowire contacts, Nanotechnology 19 (2008) 365201.
[67] S. Pud, et al., Features of transport in ultrathin gold nanowire structures, Small 9 (2013) 846–852.
[68] Bulmer, J. CNT transport database. Mendeley Data Preprint at https://doi.org/10.17632/4hhtf2vzs6.1.
[69] D.E. Tsentalovich, et al., Relationship of extensional viscosity and liquid crystalline transition to length distribution in carbon nanotube solutions, Macromolecules 49 (2016) 681–689.
[70] N. sisl Papior, Preprint at. https://doi.org/10.5281/zenodo.597181, 2023.
[71] N. Papior, N. Lorente, T. Frederiksen, A. Garcia, M. Brandbyge, Improvements on non-equilibrium and transport green function techniques: the next-generation transiesta, Comput. Phys. Commun. 212 (2017) 8–24.
[72] A. Zettl, Extreme oxygen sensitivity of electronic properties of carbon nanotubes, Science (1979) 287 (2000) 1801–1804.
[73] A. Lekawa-Raus, et al., Influence of atmospheric water vapour on electrical performance of carbon nanotube fibres, Carbon N Y 87 (2015) 18–28.
[74] J. Bulmer, et al., Microwave conductivity of sorted CNT assemblies, Sci. Rep. 4 (2014) 3762.
[75] C. Rutherglen, P. Burke, Nanoelectromagnetics: circuit and electromagnetic properties of carbon nanotubes, Small 5 (2009) 884–906.
[76] X. Wang, et al., Magnetotransport in type-enriched single-wall carbon nanotube networks, Phys. Rev. Mater. 2 (2018) 116001.
[77] A.B. Kaiser, G.U. Flanagan, D.M. Stewart, D. Beaglehole, Heterogeneous model for conduction in conducting polymers and carbon nanotubes, Phys. Rev. B 57 (1998) 1418.
[78] A. Ubbelohde, Electronic properties of graphite and its crystal compounds in the direction of the c-axis, in: Proceedings of the Fifth Conference on Carbon, 1962, pp. 1–7, https://doi.org/10.1016/b978-0-08-009707-7.50005-4.
[79] T.E. Thompson, E.R. Falardeau, L.R. Hanlon, The electrical conductivity and optical reflectance of graphite-SbF5 compounds, Carbon N Y 15 (1977) 39–43.
[80] G. Kinchin, The electrical properties of graphite, Proc. R. Soc. A 217 (1953) 9–26.
[81] J. Lee, et al., Impact of carbon nanotube length on electron transport in aligned carbon nanotube networks, Appl. Phys. Lett. 106 (2015) 053110.
[82] G. Venugopal, K. Sang-Jae, Temperature dependence of transport anisotropy of planar-type graphite nanostructures fabricated by focused ion beam, J. Nanosci. Nanotechnol. 11 (2011) 296–300.
[83] M.J. Cohen, L.B. Coleman, A.F. Garito, A.J. Heeger, Electrical conductivity of tetrathiofulvalinium tetracyanoquinodimethan, Phys. Rev. B 10 (1974) 1298–1307.
[84] Lekawa-Raus A.E., et al., Quantum limits of electronic transport in nanostructured macroscopic conductors, in preparation.
[85] D.O. Shpylka, et al., The features of the magnetoresistance of carbon nanotubes modified with Fe, Ceram. Int. 48 (2022) 19789–19797.
[86] E. Cimpoiasu, V. Sandu, G.A. Levin, A. Simpson, D. Lashmore, Angular magnetoresistance of stretched carbon nanotube sheets, J. Appl. Phys. 111 (2012) 123721.
[87] I.V. Ovsienko, et al., Magnetoresistance of multi-walled carbon nanotubes modified with iron, Mater. Werkst. 44 (2013) 161–166.
[88] G.T. Kim, et al., Magnetoresistance of an entangled single-wall carbon-nanotube network, Phys. Rev. B Condens. Matter 58 (1998) 16064–16069.
[89] L. Piraux, F. Araujo, T. Bui, M. Otto, J. Issi, Two-dimensional quantum transport in highly conductive carbon nanotube fibers, Phys. Rev. B Condens. Matter 92 (2015) 085428.
[90] T.F. Rosenbaum, Low-temperature magnetoresistance of a disordered metal, Phys. Rev. Lett. 47 (1981) 1758–1761.
[91] M. Reghu, Y. Vakkparta, Y. Cao, D. Moses, Pressure dependence of the conductivity and magnetoconductance in oriented iodine-doped polyacetylene, Phys. Rev. B 49 (1994) 162–170.
[92] T. Ando, Theory of electronic states and transport in carbon nanotubes, J. Phys. Soc. Japan 74 (2005) 777–817.
[93] N. Nemec, G. Cuniberti, Hofstadter butterflies of carbon nanotubes: pseudofractality of the magnetoelectronic spectrum, Phys. Rev. B Condens. Matter 74 (2006) 165411.
[94] S. Nanot, et al., Propagative landau states and fermi level pinning in carbon nanotubes, Phys. Rev. Lett. 103 (2009) 256801.
[95] S. Roche, S. Roche, G. Dresselhaus, M.S. Dresselhaus, R. Saito, Aharonov-Bohm spectral features and coherence lengths in carbon nanotubes, Phys. Rev. B Condens. Matter 62 (2000) 16092–16099.
[96] H. Ajiki, T. Ando, Energy bands of carbon nanotubes in magnetic fields, J. Phys. Soc. Japan 65 (1996) 505–514.
[97] B.I. Shklovskii, A.L. Efros, Variable-range hopping conduction, in: Electronic Properties of Doped Semiconductors, Springer, Berlin, Heidelberg, Berlin, 1984, pp. 202–227, https://doi.org/10.1007/978-3-662-02403-4_9.
[98] H. Tokumoto, R. Mansfield, M.J. Lea, Correlation effect in variable range hopping in n-InSb, Solid State Commun. 35 (1980) 961–964.
[99] O. Ivanov, M. Yaprintsev, Variable-range hopping conductivity in Lu-doped Bi 2 Te 3, Solid State Sci. 76 (2018) 111–117.
[100] D.E. Soule, Magnetic field dependence of the Hall effect and magnetoresistance in graphite single crystals, Phys. Rev. 112 (1958) 698–707.
[101] L.D. Woolf, J. Chin, Y.R. Lin-Liu, H. Ikezi, Electrical transport properties of benzene-derived graphite fibers, Phys. Rev. B 30 (1984) 861–869.
[102] K. Noto, T. Tsuzuku, A simple two-band theory of galvanomagnetic effects in graphite in relation to the magnetic field azimuth, Jpn. J. Appl. Phys. 14 (1975) 46–51.
[103] J. Xu, et al., Extended Kohler's rule of magnetoresistance, Phys. Rev. X 11 (2021) 41029.
[104] X.X. Xi, et al., MgB2 thin films by hybrid physical-chemical vapor deposition, Phys. C: Superconduct. Appl. 456 (2007) 22–37.
[105] W. Lang, Effect of microcrystalline structure on the transport properties of pristine and AsF5-intercalated, highly-oriented, pyrolytic graphite, Synth. Met. 34 (1989) 491–496.
[106] M.A. Hermosilla-Palacios, et al., Carrier density and delocalization signatures in doped carbon nanotubes from quantitative magnetic resonance, Nanoscale Horiz. 9 (2023) 278–284.
[107] W.D. Lee, G.P. Davis, F.L. Vogel, G.P. Davist, F. Lincoln Vogel, Electrical resistivity and magnetoresistance of carbon/graphite fibers intercalated with nitric acid and arsenic pentafluoride, Carbon N Y 23 (1985) 731–737.
[108] X. Zhou, J.Y. Park, S. Huang, J. Liu, P.L. McEuen, Band structure, phonon scattering, and the performance limit of single-walled carbon nanotube transistors, Phys. Rev. Lett. 95 (2005) 146805.
[109] M.C. Beard, J.L. Blackburn, M.J. Heben, Photogenerated free carrier dynamics in metal and semiconductor single-walled carbon nanotube films, Nano Lett. 8 (2008) 4238–4242.
[110] Y. Yomogida, et al., Hall effect in gated single-wall carbon nanotube films, Sci. Rep. 12 (2022) 101.
[111] S. Ilani, P.L. McEuen, Electron transport in carbon nanotubes, Annu. Rev. Condens. Matter Phys. 1 (2010) 1–25.
[112] P.L. McEuen, J. Park, Electron transport in single-walled carbon nanotubes, MRS Bull. 272 (2004).
[113] J.H. Han, M.S. Strano, Room temperature carrier transport through large diameter bundles of semiconducting single-walled carbon nanotube, Mater. Res. Bull. 58 (2014) 1–5.
[114] V. Perebeinos, J. Tersoff, P. Avouris, Electron-phonon interaction and transport in semiconducting carbon nanotubes, Phys. Rev. Lett. 94 (2005) 086802.
[115] T.C. Chieu, G. Timp, M.S. Dresselhaus, M. Endo, A.W. Moore, High-field magnetoresistance measurements on highly ordered graphite fibers, Phys. Rev. B 27 (1983) 3686–3696.
[116] R. Allgaier, Magnetoresistance in PbS, PbSe, and PbTe at 295°, 77.4°, and 4.2°K, Phys. Rev. 112 (1958) 828–836.
[117] H.K. Pal, D.L. Maslov, Necessary and sufficient condition for longitudinal magnetoresistance, Phys. Rev. B 81 (2010) 214438.
[118] Y. Mitani, Y. Fuseya, Large Longitudinal Magnetoresistance of Multivalley Systems, J. Phys.: Condens. Matter 32 (2020) 345802.
[119] J.A. Woollam, The longitudinal magnetoresistance of graphite ϱzz(Hz) in high magnetic fields, Solid State Commun. 9 (1971) 1581–1585.
[120] D. Liang, J. Du, X.P.A. Gao, Anisotropic magnetoconductance of a InAs nanowire: angle-dependent suppression of one-dimensional weak localization, Phys. Rev. B Condens. Matter 81 (2010) 153304.
[121] D. Liang, M.R. Sakr, X.P.A. Gao, One-dimensional weak localization of electrons in a single InAs nanowire, Nano Lett. 9 (2009) 1709–1712.
[122] P. Roulleau, et al., Suppression of weak antilocalization in InAs nanowires, Phys. Rev. B Condens. Matter 81 (2010) 155449.
[123] Y.Z. Kovdrya, V.A. Nikolaenko, S.P. Gladchenko, Weak localization effects in a quasi-one-dimensional electron system over liquid helium, JETP Lett. 73 (2001) 465–469.
[124] S. Ahn, et al., Magnetotransport in iodine-doped single-walled carbon nanotubes, Phys. Rev. B Condens. Matter 80 (2009) 165426.
[125] M. Baxendale, V.Z. Mordkovich, S. Yoshimura, R.P.H. Chang, Magnetotransport in bundles of intercalated carbon nanotubes, Phys. Rev. B Condens. Matter 56 (1997) 2161–2165.
[126] W. Schirmacher, Quantum-interference magnetoconductivity in the variable-range-hopping regime, Phys. Rev. B 41 (1990) 2461–2468.
[127] A. Frydman, Z. Ovadyahu, Spin and quantum interference effects in hopping conductivity, Solid State Commun. 94 (1995) 745–749.
[128] U. Sivan, O. Entin-Wohlman, Y. Imry, Orbital magnetoconductance in the variable-range hopping regime, Phys. Rev. Lett. 60 (1988) 1566–1569.
[129] Y. Yosida, I. Oguro, Variable range hopping conduction in multiwalled carbon nanotubes, J. Appl. Phys. 83 (1998) 4985–4987.
[130] M. Radosavljević, J. Lefebvre, A.T. Johnson, High-field electrical transport and breakdown in bundles of single-wall carbon nanotubes, Phys. Rev. B Condens. Matter 64 (2001) 241307.
[131] S.H. Jhang, et al., Direct observation of band-gap closure for a semiconducting carbon nanotube in a large parallel magnetic field, Phys. Rev. Lett. 106 (2011) 096802.
[132] G. Fedorov, et al., Magnetically induced field effect in carbon nanotube devices, Nano Lett. 7 (2007) 960–964.
[133] S. Zaric, E. Al, Optical signatures of the Aharonov-Bohm phase in single-walled carbon nanotubes, Science (1979) 304 (2004) 1129–1131.
[134] W. Izumida, K. Sato, R. Saito, Spin-orbit interaction in single wall carbon nanotubes: symmetry adapted tight-binding calculation and effective model analysis, J. Phys. Soc. Japan 78 (2009) 074707.
[135] S.H. Jhang, et al., Spin-orbit interaction in chiral carbon nanotubes probed in pulsed magnetic fields, Phys. Rev. B Condens. Matter 82 (2010) 041404.

[136] C. Zamora-Ledezma, et al., Conductivity anisotropy of assembled and oriented carbon nanotubes, Phys. Rev. E - Stat. Nonlinear Soft Matter Phys. 84 (2011) 062701.
[137] F. Pawlek, D. Rogalla, The electrical resistivity of silver, copper, aluminium, and zinc as a function of purity in the range 4–298° K, Cryogenics (Guildf) 6 (1966) 40.
[138] Simon N.J., Drexler E.S., Reed R.P., Properties of copper and copper alloys at cryogenic temperatures. Final report, National Institute of Standards and Technology (NIST), 1992.
[139] A. Znidarsic, et al., Spatially resolved transport properties of pristine and doped single-walled carbon nanotube networks, J. Phys. Chem. C 117 (2013) 13324–13330.
[140] V. Sivasubramaniyam, S. Ramasamy, M. Venkatraman, G. Gatto, A. Kumar, Carbon nanotubes as an alternative to copper wires in electrical machines: a review, Energies 16 (2023), https://doi.org/10.3390/en16093665. Preprint at.
[141] A. Lekawa-Raus, J. Patmore, L. Kurzepa, J. Bulmer, K. Koziol, Electrical properties of carbon nanotube based fibers and their future use in electrical wiring, Adv. Funct. Mater. 24 (2014) 3661–3682.
[142] M. Rdest, D. Janas, Carbon nanotube films for energy applications, Energies 14 (2021) 1890.
[143] M. Tehrani, Advanced electrical conductors: an overview and prospects of metal nanocomposite and nanocarbon based conductors, Phys. Status Solidi (A) Appl. Mater. Sci. 218 (2021) 2000704.
[144] A. Pendashteh, A. Mikhalchan, T. Blanco Varela, J.J. Vilatela, Opportunities for nanomaterials in more sustainable aviation, Discover Nano. 19 (2024), https://doi.org/10.1186/s11671-024-04087-5. Preprint at.
[145] M. Pasquali, C. Mesters, We can use carbon to decarbonize—and get hydrogen for free, Proc. Natl. Acad. Sci. U.S.A. 118 (2021) e2112089118, 31.
[146] J. Murday, D. Dominguez, J. Moran, W. Lee, R. Eaton, An assessment of graphitized carbon fiber use for electrical power transmission, Synth. Met. 9 (1984) 397–424.
[147] Y. Wang, et al., Research progress of overhead conductors with carbon fiber composite core, J. Comput. Methods Sci. Eng. 24 (2024) 3557–3562.
[148] K.H. Ryu, et al., Core-sheath composite electric cables with highly conductive self-assembled carbon nanotube wires and flexible macroscale insulating polymers for lightweight, metal-free motors, Adv. Compos. Hybrid Mater. 8 (2025) 230.
[149] J.N. Chapman, et al., Flightweight carbon nanotube magnet technology. www.sti.nasa.gov, 2003.
[150] G. Aliana-Cervera, D. Mattia, C. Pasquino, Carbon nanotube wires for accelerator applications, Mater. Des. 258 (2025) 114606.
[151] D. Janas, A. Cabrero-Vilatela, J. Bulmer, L. Kurzepa, K.K. Koziol, Carbon nanotube wires for high-temperature performance, Carbon 64 (2013) 305–314.
[152] D. Janas, A.C. Vilatela, K.K.K. Koziol, Performance of carbon nanotube wires in extreme conditions, Carbon 62 (2013) 438–446.